Computer Modeling in Engineering & Sciences

Tech Science Press

https://doi.org/10.32604/cmes.2026.087312

ARTICLE

An Integrated Design Framework for Additively Manufactured Multi-Axial Parts: Topology Optimization, Multibody Dynamic Load Extraction and Surface-Topography-Based Fatigue Correction

Yuwei Liu[1], **Yuhui Liu**[1], **Zhengkun Cheng**[2,*], **Yang Zhao**[3] **and Lulu Nie**[2]

[1]School of Mechanical and Electrical Engineering, China University of Mining and Technology-Beijing, Beijing, China
[2]School of Automotive and Transportation Engineering, Shenzhen Polytechnic University, Shenzhen, China
[3]Department of Construction, Environment and Engineering, Technological and Higher Education Institute of Hong Kong, Hong Kong, China

*Corresponding Author: Zhengkun Cheng. Email: zhengkun2005@163.com

Received: 22 June 2026; Accepted: 14 September 2026; Published: 21 October 2026

ABSTRACT: This work proposes a universal closed-loop design and fatigue evaluation framework for additive manufacturing (AM) multi-axial lightweight load-bearing components, integrating solid isotropic material with penalty (SIMP)-based topology optimization, multibody dynamics load spectrum extraction, and surface topography-corrected fatigue life prediction. The Formula Student China (FSC) racing upright is adopted as a typical engineering carrier to demonstrate the complete workflow. Topology optimization targeting extreme multi-load conditions is implemented via the SIMP method under a volume fraction constraint of 0.3, followed by AM-process-compliant geometric reconstruction and static strength verification. A full-vehicle RecurDyn model extracts load spectra that have been validated through vehicle testing with a Pearson correlation coefficient of 0.9643. The assessment of baseline fatigue damage is conducted using the critical plane method and Miner's rule in nCode DesignLife. A fatigue notch factor K_f corrects the Manson–Coffin equation, yielding a strain–life model that accounts for surface wavelength, roughness, and measured topography. The optimized uprights meet static strength requirements, with maximum von Mises stresses of 175.38 MPa for the front upright and 184.63 MPa for the rear upright under braking conditions, both well below the allowable stress of 350 MPa; the baseline maximum cumulative fatigue damage reaches 6.95×10^{-4} for the front upright and 2.81×10^{-6} for the rear upright, both far below the failure threshold of 1. Quantitative results indicate that, at a fixed R_a = 5 μm, reducing the surface wavelength from 1000 to 200 μm increases the fatigue notch factor K_f from 1.090 to 1.303 and raises maximum fatigue damage by approximately 59% (front upright); at a fixed wavelength of 1000 μm, increasing R_a from 20 to 100 μm elevates K_f from 1.359 to 2.795 and amplifies maximum damage by over 300% (front upright). Shorter wavelengths and higher roughness exacerbate damage, while identical R_a values with varying micro-topographies produce markedly different fatigue lives, highlighting the inadequacy of relying solely on R_a. Integrating topology optimization with surface topography-based life correction, the proposed framework supports the lightweight design and fatigue life evaluation of uprights and similar components in automotive, aerospace, and robotic systems.

KEYWORDS: Topology optimization; AM lightweight components; multibody dynamics; surface roughness; fatigue notch factor; strain-life correction

Copyright © 2026 The Authors. Published by Tech Science Press. This work is licensed under a Creative Commons Attribution 4.0 International License, which permits unrestricted use, distribution, and reproduction in any medium, provided the original work is properly cited.

1 Introduction

Multi-axial cyclic load-carrying lightweight components are widely adopted across automotive, aerospace and robotic systems, including vehicle suspension knuckles, aircraft connecting lugs and robot joint supports. These structures bear complex alternating loads and require simultaneous lightweight design and long fatigue durability, forming a universal engineering contradiction for AM. The steering upright of FSC race cars is selected as a typical representative of such multi-load AM safety-critical parts, which connects suspension linkages and wheel hubs under coupled road excitation, braking torque and lateral steering forces. Its lightweight efficiency and fatigue performance directly reflect the comprehensive performance of the proposed integrated design method. In racing car design, balancing extreme lightweighting with sufficient fatigue durability presents a fundamental engineering challenge. If material removal is pursued in isolation without accounting for the resultant degradation in fatigue strength, cracks may initiate prematurely within the upright under the service alternating loads, potentially leading to catastrophic structural failure and severely jeopardizing safe racing operations. As formula student competitions become increasingly competitive, the demand for a robust design methodology that systematically tackles both lightweighting and fatigue life assessment has grown more urgent.

Structural topology optimization is a systematic conceptual design approach that autonomously identifies the optimal load transfer path within a prescribed design space under given loads, serving as a powerful theoretical tool for lightweight component design [1–5]. The density-based SIMP method introduces a penalization factor that drives element relative densities toward 0 or 1, thereby producing a well-defined material distribution, and has been extensively validated in the lightweight design of automotive components [6–10]. Conventional topology optimization methods are typically founded on ideally smooth geometric models and the presumption of homogeneous, isotropic material behavior. Their ability to adequately represent the characteristics of the actual manufacturing process is insufficient, particularly for the surface geometric defects and microstructural inhomogeneities induced by AM. This simplification leads to a non-negligible deviation between the theoretical performance of the optimized configuration and its actual in-service behavior [11–13].

AM facilitates the near-net-shape fabrication of geometrically complex structures through layer-by-layer deposition, providing an ideal process route for producing topology-optimized designs. However, the intrinsic layered nature of this process inevitably introduces micro-scale geometric imperfections on the surface of the part, such as rough topography, partially unmelted particles, and stair-step effects. These surface defects act as stress concentrators, generating considerable localized stresses that serve as preferential sites for fatigue crack initiation [14–16]. Numerous studies have demonstrated that the fatigue strength of additively manufactured metallic parts is frequently substantially lower than their static strength, with surface roughness being a dominant contributing factor [17].

The classic Manson–Coffin equation serves as the foundational model for describing the strain–life relationship of materials in fatigue life prediction [18,19]. However, the material constants in this equation are conventionally calibrated from fatigue tests on standard smooth specimens. Applying such constants directly to additively manufactured parts with rough surfaces would inevitably yield non-conservative life predictions, as the stress concentration effects arising from surface topography are entirely disregarded [20–24]. To address this limitation, the fatigue notch factor K_f has been introduced to specifically adjust the elastic segment of the strain–life (ε–N) curve [25–28]. This approach effectively reflects the degradation of high-cycle fatigue performance caused by stress concentrations originating from surface micro-geometric features [29,30]. Simultaneously, multibody dynamics simulation provides an efficient means for acquiring the dynamic load spectra of components under actual operating conditions [31–33]. Constructing a full-vehicle multibody dynamics model enables the precise extraction of load–time histories for the

upright under typical track circumstances, supplying reliable boundary conditions for subsequent fatigue analysis [34–36].

Current research on topology optimization and surface-related fatigue prediction exists in two isolated branches: topology optimization with ideal smooth geometric static verification, and independent material-level studies on surface roughness fatigue degradation. While Boursier Niutta et al. proposed a defect-driven topology optimization for fatigue design (TopFat) method to integrate AM defect characteristics into fatigue-focused topology optimization [37], no existing work integrates four core modules into a unified closed-loop workflow: process-constrained topology optimization, multi-body dynamic real load spectrum extraction, critical-plane multi-axial fatigue damage calculation, and surface-topography-based strain-life correction. This separation of research initiatives results in a critical disconnect across the entire engineering workflow, from conceptual design to reliable fatigue life prediction, for additively manufactured uprights.

Within this framework, the novelty lies in the systematic integration of these four modules into a unified closed-loop workflow. Specifically, the topology optimization module adopts a SIMP formulation with a volume fraction constraint and a symmetry constraint, and AM manufacturability is enforced through a dedicated geometric reconstruction step; the multibody dynamics load spectrum extraction follows standard vehicle dynamics procedures; the multi-axial fatigue damage calculation employs the critical plane approach and Miner's linear damage accumulation rule; and the surface-topography-based strain-life correction extends the classical Manson–Coffin equation through the introduction of the fatigue notch factor. While each individual methodology is adapted from established literature, their combined application to the holistic design and fatigue life evaluation of an FSC upright constitutes the original contribution of this work.

2 Topology Optimization Design of Racing Uprights

To provide readers with an overarching view of the proposed closed-loop workflow at the outset, the integrated design and analysis procedure is schematically illustrated in Fig. 1. The framework comprises four sequentially coupled modules: (i) SIMP-based topology optimization with AM-compliant geometric reconstruction; (ii) multibody dynamic load spectrum extraction validated by full-vehicle tests; (iii) baseline multi-axial fatigue damage assessment via the critical plane method; and (iv) surface-topography-corrected fatigue life prediction using the K_f-modified Manson–Coffin model. While the present section (Section 2) focuses exclusively on Module 1—the topology optimization design and static strength verification of the front and rear uprights—the subsequent sections elaborate on the remaining modules: Section 3 details Modules 2 and 3 (load spectrum acquisition and baseline fatigue analysis), and Section 4 addresses Module 4 (surface-roughness-aware life correction). This roadmap ensures that the workflow is introduced as a cohesive whole before delving into the technical specifics of each constituent step.

This section focuses on the front and rear uprights of an FSC racing car. Topology optimization for multiple load cases is carried out using the variable density method. Engineering reconstruction is subsequently executed in accordance with the specific characteristics of additive manufacturing. The robustness of the optimized structure is subsequently verified through detailed static strength checks, eventually achieving a favorable balance between weight reduction and structural performance.

2.1 Basic Principle of Topology Optimization

This article employs the topology optimization method based on the variable density approach with the SIMP model. Its core concept is to take the relative density of each element inside the design domain as a design variable. A penalty factor p is introduced to drive the material element density towards 0 or 1, yielding a distinct material distribution configuration. The fundamental assumption of the SIMP model is that the

material's elastic modulus E and the element relative density ρ_i satisfy a power-law relationship, defined as follows:

$$\begin{aligned} E(\rho_i) &= E_{\min} + \rho_i^p (E_0 - E_{\min}) \\ &= E_{\min} + \rho_i^p \Delta E \end{aligned} \tag{1}$$

where $E(\rho_i)$ corresponds to the interpolated elastic modulus of the element; E_0 denotes the initial elastic modulus of the material; $E_{\min}$ refers to a very small elastic modulus set to avoid singularity of the total stiffness matrix, generally taken as $E_{\min} = E_0/1000$; p represents the penalty factor, usually ranging from 3 to 5.

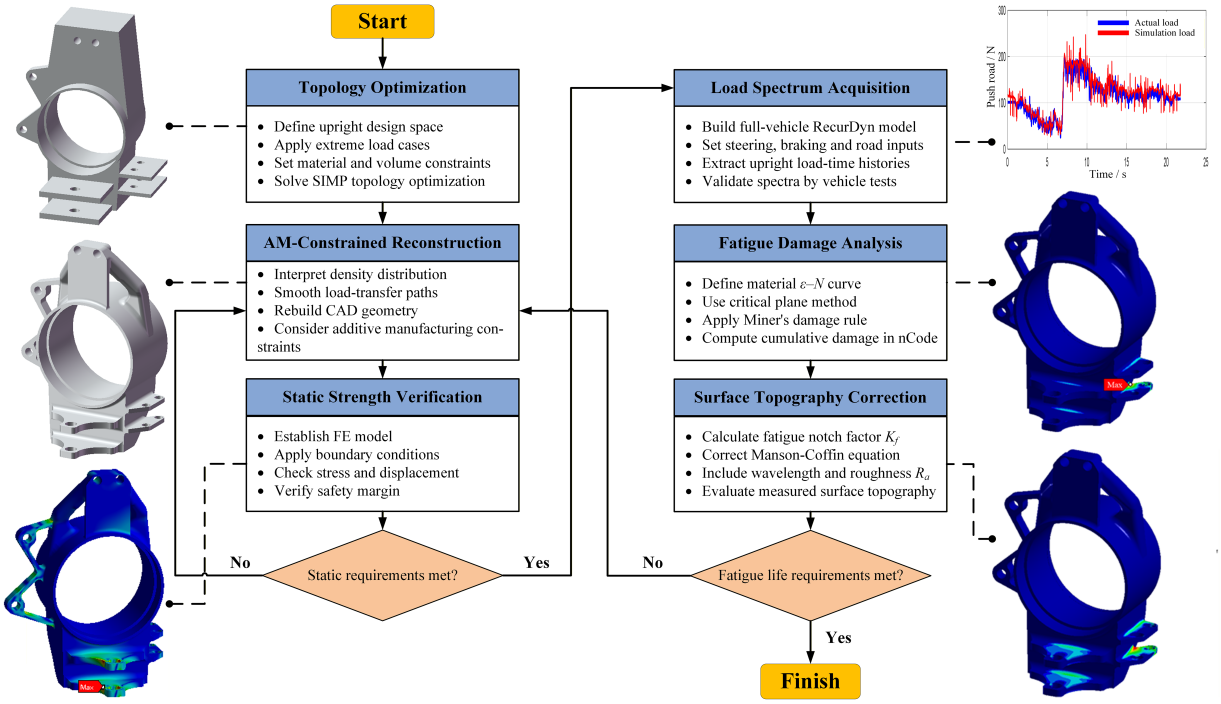


Figure 1: The procedure integrating topology optimization, additive manufacturing and fatigue analysis for FSC racing uprights.

The objective function of topology optimization is to minimize the weighted compliance under multiple load cases, i.e., to maximize stiffness. The constraints include a volume fraction constraint and a symmetry geometric constraint to ensure shape symmetry and manufacturability of the upright. The mathematical model can be formulated as:

$$\min_{\rho} C_w(\rho) = \sum_{k=1}^{M} w_k \mathbf{F}_k^T \mathbf{U}_k(\rho)$$

$$\text{geo} = \text{symmetry}$$

$$\text{S.t.} \begin{cases} V(\rho)/V_0 \le f_v \\ \mathbf{K}(\rho)\mathbf{U}_k = \mathbf{F}_k, k = 1, 2, \ldots, M \\ 0 < \rho_{min} < \rho_i \le 1, i = 1, 2, \ldots, n \end{cases} \tag{2}$$

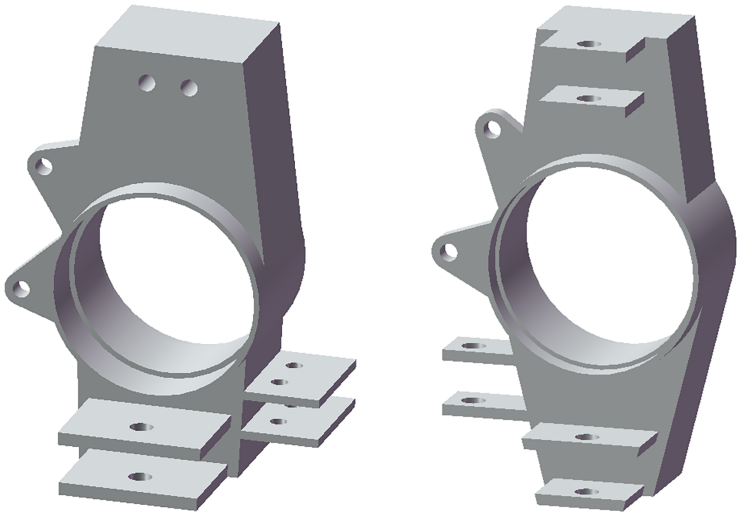
where $C_w(\rho)$ stands for the total weighted compliance; w_k gives the weighting factor for the k-th load case, satisfying $\sum_{k=1}^{M} w_k = 1$; $\mathbf{K}(\rho)$ represents the global stiffness matrix; $\mathbf{F}_k$ and $\mathbf{U}_k$ are respectively the global load vector and nodal displacement vector for the k-th load case; $V(\rho)$ designates the optimized structural volume; V_0 is the total volume of the initial design domain; f_v defines the volume fraction constraint ($0 < f_v < 1$, here $f_v = 0.3$). To prevent singularity of the finite element stiffness matrix, a minimum relative density ρ_{min} is introduced, typically taken as 0.001.

2.2 Establishment and Solution of the Topology Optimization Model

2.2.1 Design Space and Load Case Determination

The maximum solid model of the upright is initially established as the design space. This is based on the positions of the mounting bolt holes and the boundary conditions of surrounding components, as illustrated in Fig. 2. To balance computational efficiency and geometric adaptability, a hybrid discretization strategy is employed, using predominantly hexahedral elements supplemented by tetrahedral elements. The global element dimension is controlled at 2 mm. Essential functional features, such as mounting holes and mating surfaces, are designed as non-design regions. This guarantees that their geometry and functionality remain unaltered by optimization. Fig. 3 illustrates the mesh models of the uprights.

In the topology optimization, these three extreme load cases are assigned equal weighting factors, and a multi-case weighted compliance minimization formulation is adopted. The load components listed in Table 1 were obtained from simulations of the upright's idealized loading conditions under each extreme maneuver during the initial design phase, which is consistent with the standard workflow of early-stage topology optimization [38].



(**a**) (**b**)

Figure 2: Maximum solid models of the uprights. (**a**) Front upright; (**b**) Rear upright.

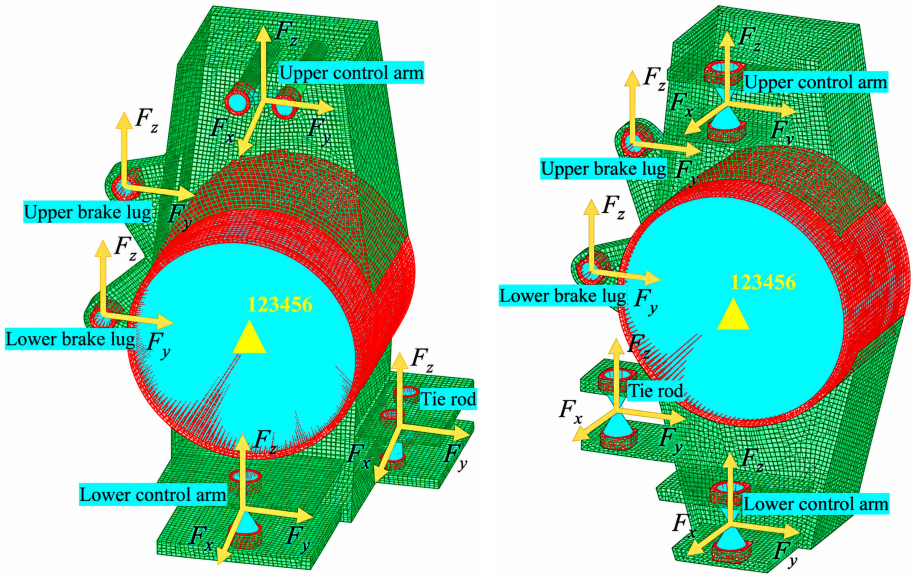


Figure 3: Finite element models for topology optimization of the uprights. (**a**) Front upright; (**b**) Rear upright.

Table 1: Ultimate load cases for the front and rear uprights.

Uprights	Ultimate Load Cases	Connection Point	F_x/N	F_y/N	F_z/N
Front	Braking	Upper control arm	709	−690	−509
		Tie rod	24	629	−13
		Lower control arm	−1282	281	−30
		Upper brake lug	0	1200	1000
		Lower brake lug	0	−1200	1000
	Right turn	Upper control arm	397	448	−347
		Tie rod	−71	−70	−10
		Lower control arm	−581	792	−11
	Acceleration	Upper control arm	748	−185	1102
		Tie rod	21	220	−10
		Lower control arm	100	−601	−941
Rear	Braking	Upper control arm	−636	200	394
		Tie rod	−255	798	52
		Lower control arm	430	1007	−78
		Upper brake lug	0	1200	1000
		Lower brake lug	0	−1200	1000
	Right turn	Upper control arm	−151	185	291
		Tie rod	185	230	21
		Lower control arm	−231	−265	27
	Acceleration	Upper control arm	−517	254	940
		Tie rod	−407	1190	26
		Lower control arm	−483	1013	−20

2.2.2 Material Properties and Constraints

The uprights are made of 7075-T6 aluminum alloy, which offers a high specific strength and meets the performance requirements of racing components. The material properties are listed in Table 2 [39].

Table 2: Material properties of 7075-T6 aluminum alloy for the uprights.

Elastic Modulus/GPa	Poisson's Ratio	Density/(g/cm^3)	Yield Strength/MPa	Tensile Strength/MPa
71.7	0.33	2.81	455	525

Constraints are set according to the actual installation conditions of the upright: fixed constraints are applied at the connection holes between the upright and the wheel, restricting all degrees of freedom. Concentrated loads are exerted at the lug holes connecting the upright to the upper control arm, lower control arm, and steering tie rod. These loads correspond to the load directions of each load case, ensuring that the load transfer accurately represents the actual mechanical conditions.

2.2.3 Topology Optimization Solution and Result Analysis

The established finite element model is imported into the HyperWorks OptiStruct solver. The topology optimization is formulated using the SIMP approach. The objective is to minimize the weighted compliance of the multiple load cases, subject to a volume fraction constraint of 0.3. The design variables are the element pseudo-densities. A symmetry constraint is additionally imposed to enforce geometric symmetry of the resulting upright structure. The finite element mesh consists of second-order tetrahedral elements with a uniform element size of 2 mm. Upon completion of the solution, the original topology optimization configurations of the front and rear uprights are obtained, as shown in Fig. 4. These configurations exhibit clear load transfer paths. Material is predominantly distributed in critical load-transmitting regions, while non-critical regions are removed, so achieving the lightweight design goal.

The original topology optimization configurations exhibit irregular features, including local sharp edges and grooves. These features are not conducive to additive manufacturing and may induce local stress concentrations. To ensure manufacturability, engineering reconstruction of the original configurations is carried out, considering the characteristics of additive manufacturing. This entails smoothing local sharp edges, adding material compensation in groove regions, forming weight-reduction holes in non-critical load-bearing areas, and optimizing lug structures to augment connection strength. Fig. 5 displays the final smoothed three-dimensional structural models of the uprights.

The reconstructed upright structures are smooth and display distinct load transfer paths. The irregularities of the original topology are eliminated. The optimal material distribution is preserved, while satisfying the manufacturability criteria of additive manufacturing. Compared with the original design space, the lightweighting effect for both front and rear uprights is significant.

2.3 Static Strength Verification of the Optimized Configuration

Due to the geometrically complex shape of the racing upright, it is challenging to employ hexahedral mesh entirely. Therefore, second-order tetrahedral elements are chosen for meshing. The global mesh size is controlled at 1 mm, ensuring high solution accuracy. Fig. 6 illustrates the finite element mesh models of the front and rear uprights. The mesh is uniform and fine, capable of accurately capturing the local stress distribution. This provides a reliable model basis for static strength investigation.

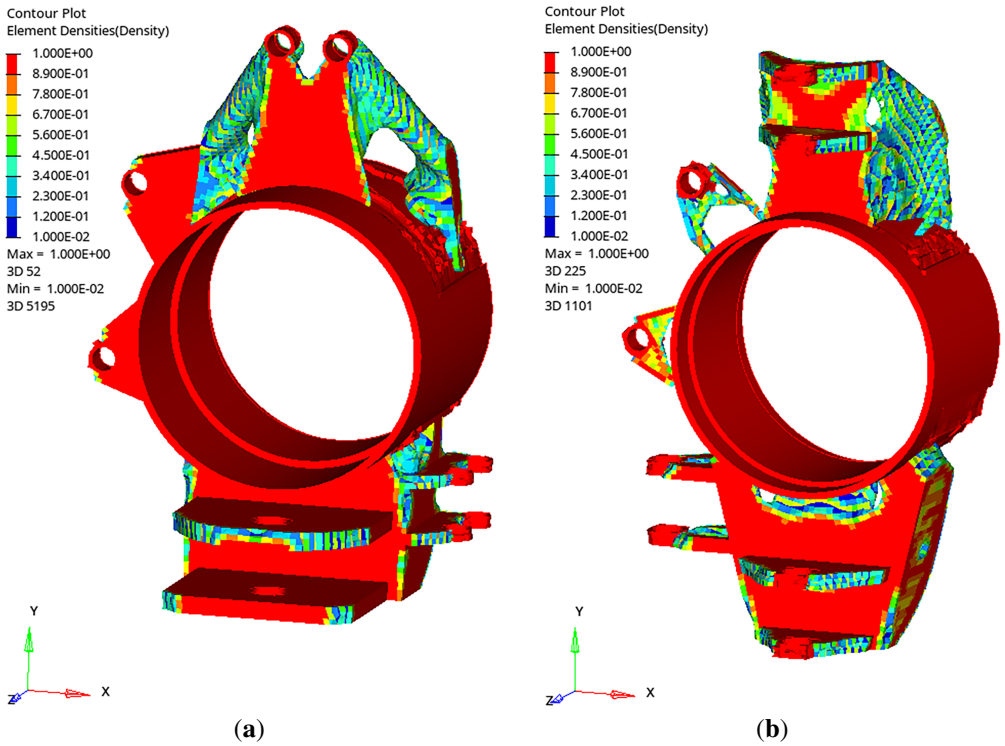


Figure 4: Topology optimization results of uprights. (**a**) Front upright; (**b**) Rear upright.

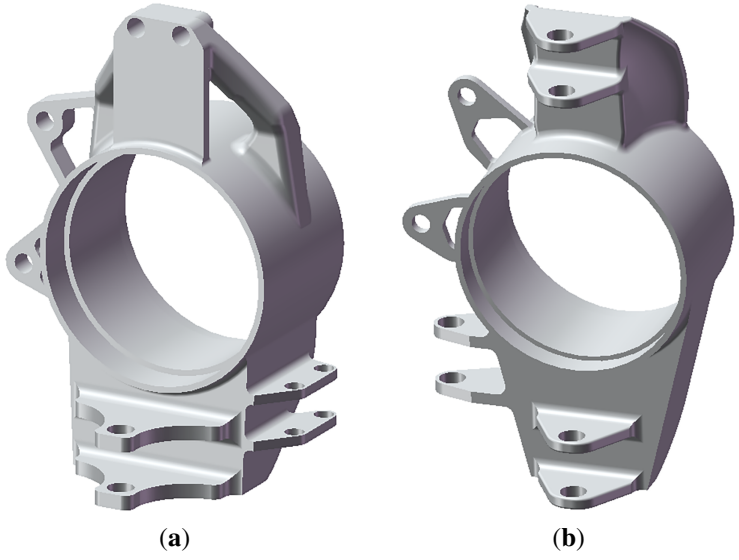


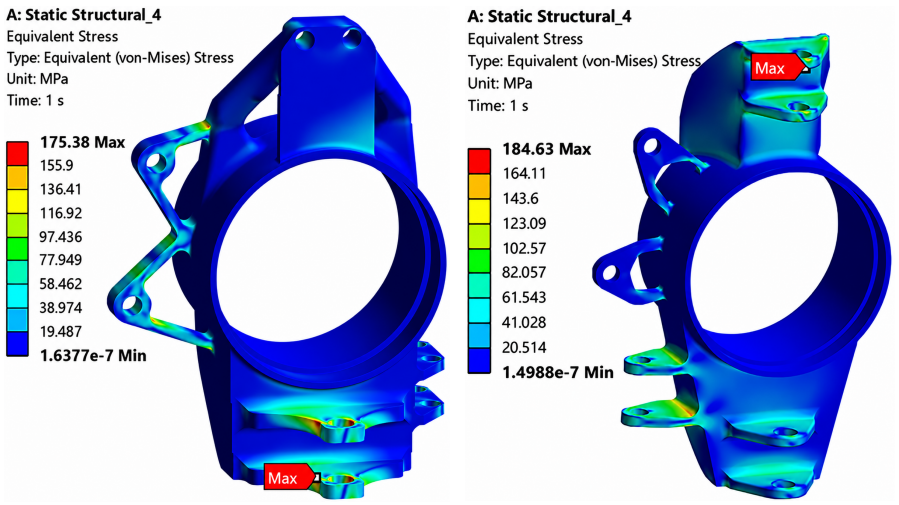
Figure 5: Smoothed 3D structural models of the uprights. (**a**) Front upright; (**b**) Rear upright.



(**a**) (**b**)

Figure 6: Finite element mesh models of the topology-optimized upright configurations. (**a**) Front upright; (**b**) Rear upright.

The braking load scenario from Table 1 is taken as the extreme load condition. All relevant loads are applied to the upright finite element model. The analysis employs the inertia relief approach and is solved in the ANSYS Mechanical Static Structural solver. Fig. 7 depicts the stress contours for the front and rear uprights under the braking conditions.



(**a**) (**b**)

Figure 7: Stress distribution contours of the uprights under braking conditions. (**a**) Front upright; (**b**) Rear upright.

As plotted in Fig. 7, under the braking condition, the maximum von Mises stress for the front upright is 175.38 MPa, whereas for the rear upright it is 184.63 MPa, both values well below the allowable stress of 350 MPa, indicating a sufficient safety margin under extreme loading. The peak stress in the front upright is located at the lower control arm junction, while in the rear upright it occurs at the lug–rib connection, slightly offset from the stress concentration point, suggesting that this region is more susceptible to cyclic strain

accumulation and may serve as a potential fatigue initiation site, warranting focused attention in subsequent detailed design and durability evaluations.

3 Fatigue Durability Analysis of the Optimized Upright Configuration

This section first acquires the dynamic load spectra of the uprights under actual operating conditions utilizing the multibody dynamics approach. The reliability of these load spectra is verified against actual vehicle test data. Multi-axial fatigue damage analysis of the uprights is performed using nCode DesignLife. The fatigue life is evaluated to provide baseline data for subsequent life correction that accounts for surface roughness.

3.1 Basic Theory of Fatigue Analysis

The strain–life method is adopted for upright fatigue life prediction. Its core formula is the Manson–Coffin equation, which decomposes the total strain amplitude into the sum of elastic and plastic strain amplitudes:

$$\varepsilon_a = \frac{\sigma_f'}{E}(2N_f)^b + \varepsilon_f'(2N_f)^c \tag{3}$$

where ε_a is the total strain amplitude; σ_f' denotes the fatigue strength coefficient; ε_f' represents the fatigue ductility coefficient; b stands for the fatigue strength exponent; and c is the fatigue ductility exponent. It should be noted that the elastic strain term asymptotically dominates in the high-cycle fatigue regime ($N_f > 10^4$–10^5 cycles), where the plastic strain term becomes negligible. Under this condition, Eq. (3) reduces to the Basquin relationship, i.e., the classical stress–life (S–N) relation. Consequently, the Manson–Coffin formulation inherently unifies both the high-cycle and low-cycle fatigue regimes within a single framework, eliminating the need to switch between separate S–N and ε–N methodologies. This unified approach is particularly suitable for the upright, which contains geometric discontinuities (e.g., lug holes and fillets) that induce local stress concentrations and possible transient plasticity even when the global nominal stress remains elastic.

The upright experiences multi-axial alternating loads during actual service. This paper adopts the critical plane method as the multi-axial fatigue damage model. This technique can precisely identify the critical plane where fatigue cracks initiate. Damage is accumulated according to Miner's linear damage accumulation:

$$D = \sum_{i=1}^{k} \frac{n_i}{N_i} \tag{4}$$

where D denotes the cumulative damage, which is dimensionless. Fatigue failure is predicted when $D \geq 1$. k is the number of stress levels; n_i represents the number of cycles actually experienced at the i-th stress S_i; and N_i is the fatigue life of the material under stress S_i.

3.2 Full-Vehicle Multibody Dynamics Modeling and Load Spectrum Extraction

3.2.1 Multibody Dynamics Software Selection and Model Simplification

The RecurDyn software has been selected to build the multibody dynamics model of the FSC racing car. This software is founded on the theory of equations of motion in relative coordinates and a fully recursive algorithm. It offers substantial benefits for handling large-scale, intricate multibody systems. The Multibody

Flexible Dynamic rigid–flexible coupling solver enables the deep integration of multibody dynamics and finite element methods, accurately simulating the dynamic response of the race car.

The complete 3D geometry model of the FSC car is imported into RecurDyn. Model simplification is performed on the premise of ensuring simulation accuracy: key components such as the frame, front and rear suspension systems, and steering system are retained; non-critical parts such as the bodywork and fasteners are removed. Counterweights are configured according to the mass parameters of the actual car. Their positions and masses are adjusted so that the total mass, center of gravity position, and moments of inertia of the simplified model remain consistent with the actual car. The complete car model is shown in Fig. 8, and the simplified vehicle dynamics model is shown in Fig. 9.

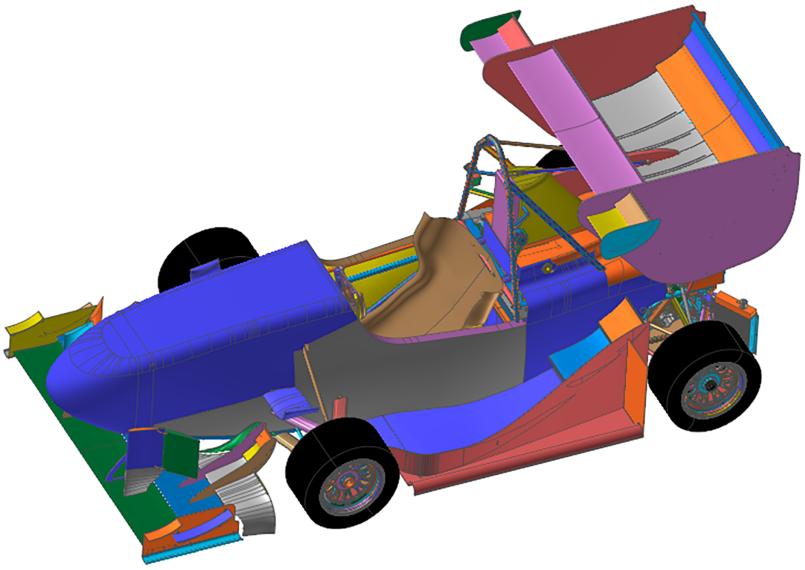


Figure 8: Complete racing car model.

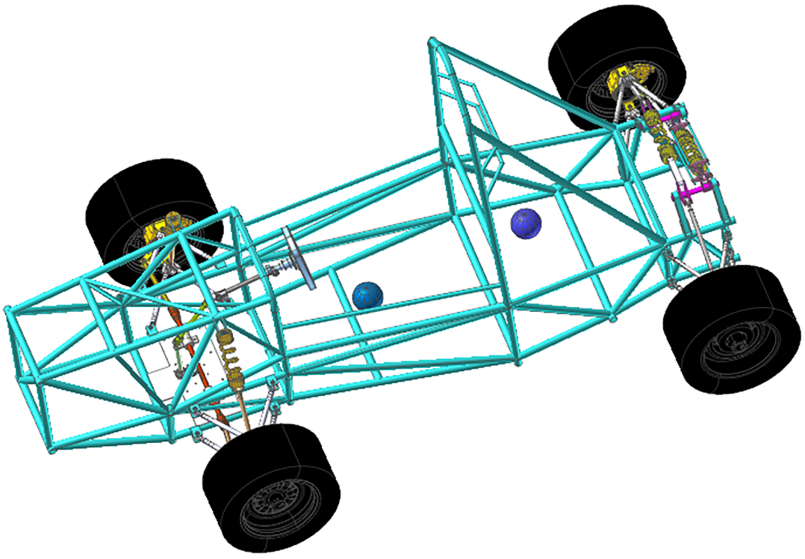


Figure 9: Simplified vehicle dynamics model.

3.2.2 Kinematic Joint Constraints and Operating Condition Setup

Corresponding kinematic joint constraints are incorporated into the simplified model according to the actual connections among components. Revolute or spherical joints are employed between control arms and the frame. Revolute joints are used between steering tie rods and the front uprights. A translational joint is applied between the rack and the vehicle body. Contact constraints are imposed between the tires and the roadway. The specific kinematic joint constraints are listed in Table 3.

Table 3: Kinematic joint constraints of the simplified full-vehicle model.

Joint Type	No.	Connected Parts
Spherical Joint	1	Steering rack–Steering tie rod 1
	2	Steering rack–Steering tie rod 2
Revolute Joint	3	Frame–Steering column gear
	4	Frame–Steering gear
	5	Frame–Steering wheel
	6	Steering tie rod 1–Left front upright
	7	Steering tie rod 2–Right front upright
Fixed	8	Steering wheel–Steering motor column
	9	Steering motor column–Steering motor joint
Translational Joint	10	Frame–Steering rack
Universal	11	Steering motor joint–Steering column
	12	Steering column–Steering column gear
Contact	13	Road surface–Left front wheel
	14	Road surface–Left rear wheel
	15	Road surface–Right front wheel
	16	Road surface–Right rear wheel
	17	Steering column gear–Encoder synchronizer gear
	18	Encoder synchronizer gear–Steering rack
Force	19	Decoupled anti-roll damper mount 1–Decoupled anti-roll damper mount 2
	20	Decoupled damper mount 1–Decoupled damper mount 2
	21	Front suspension damper left mount 1–Front suspension damper left mount 2
	22	Front suspension damper right mount 1–Front suspension damper right mount 2

The simplified vehicle model with kinematic joints and the detailed distribution of joints in the front and rear suspensions are depicted in Figs. 10 and 11, respectively. The circled numbers in Figs. 10 and 11 denote the serial numbers of the kinematic joints listed in Table 3. Each kinematic joint accurately represents the kinematic characteristics of the suspension and steering systems. This ensures that the model accurately reproduces the kinematic and dynamic behaviors of the racing car.

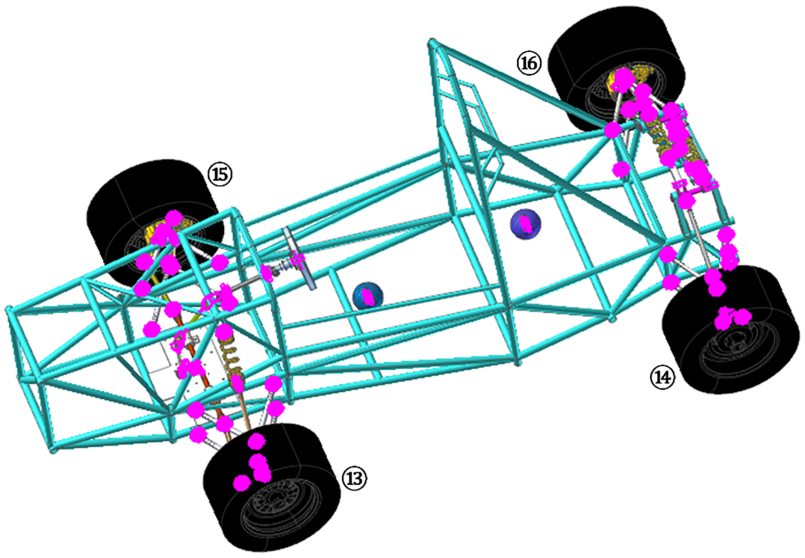


Figure 10: Simplified vehicle model with kinematic joints.

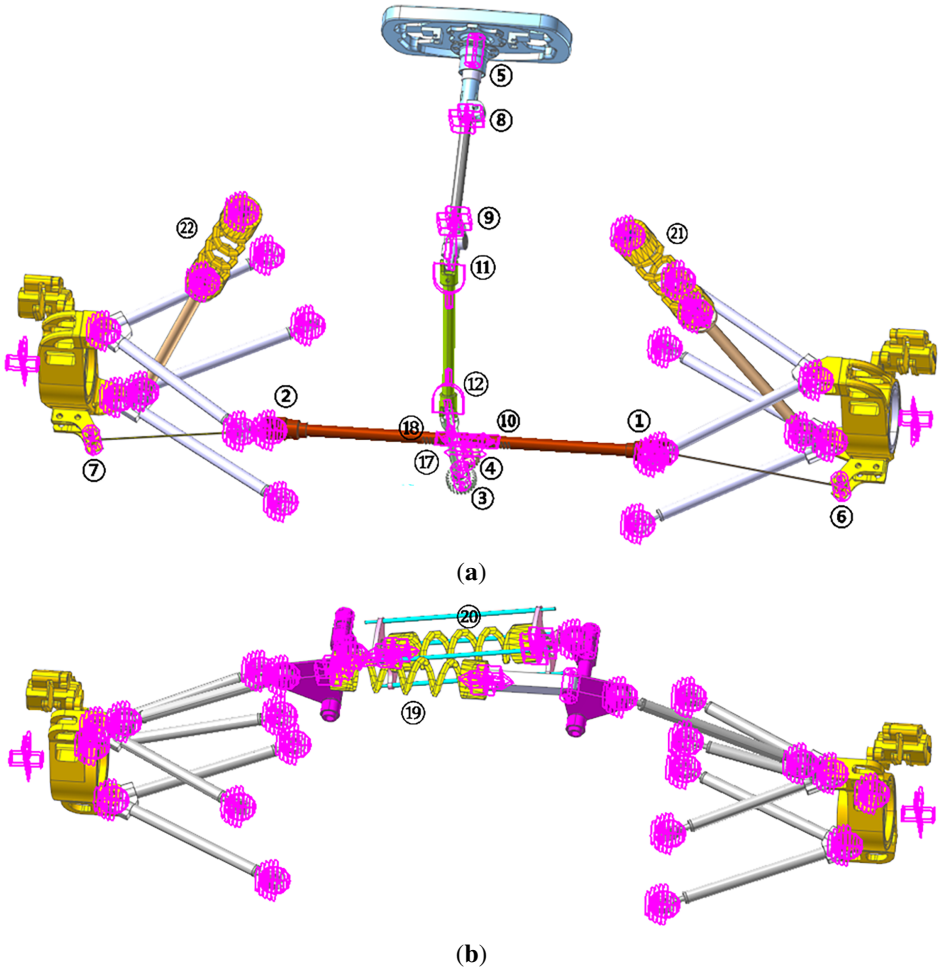


Figure 11: Distribution of kinematic joints in the front and rear suspension systems. (**a**) Front suspension joints; (**b**) Rear suspension joints.

Based on the FSC competition rules, the figure-eight track condition is designated as the typical load case for upright fatigue analysis. This condition possesses clearly delineated kinematic boundaries and periodic load characteristics. It can efficiently induce fatigue damage accumulation in the uprights under a multi-axial stress state. The schematic diagram of the figure-eight track is plotted in Fig. 12. The track consists of two concentric circles arranged in a figure-eight pattern. The distance between the centers of the two circles is 18.25 m. The inner circle diameter is 15.25 m, the outer circle diameter is 21.25 m, and the track width is 3 m.

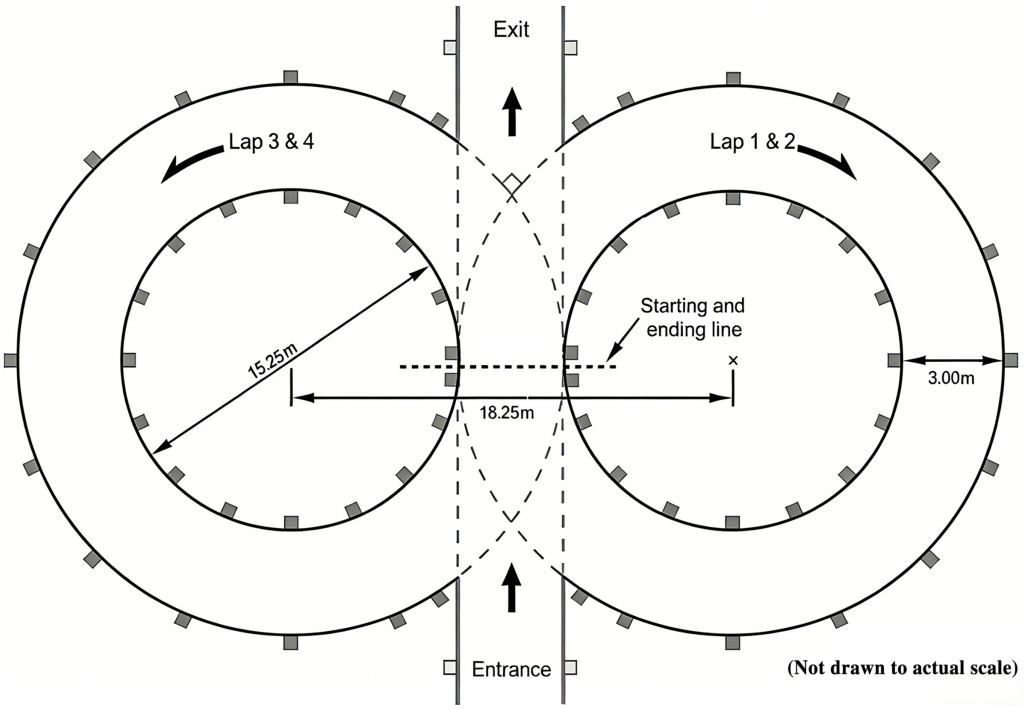


Figure 12: Schematic diagram of the figure-eight track.

The simulation condition in RecurDyn is established as follows. The vehicle initially turns right for two laps, then turns left for two laps, while maintaining a constant speed. The steering wheel angle function governs the front wheel steering. The tire speed is prescribed to sustain a constant vehicle velocity. Reaction force time histories are extracted from the kinematic joints connecting to the upper control arm, lower control arm, and steering tie rod. These temporal histories serve as the load spectra for the uprights.

3.2.3 Upright Load Spectrum Extraction Results

Because the figure-eight track is left–right symmetric, the force states of the left and right uprights are identical. Therefore, only the load spectra of the right front and right rear uprights are extracted. The results are shown in Fig. 13.

Fig. 13a shows the load spectrum for the right front upright, whereas Fig. 13b depicts that for the right rear upright. The data display the load time histories at the junctions of the upper control arm, lower control arm, and steering tie rod. The loads exhibit distinct periodic variations, aligned with the cyclic motion characteristics of the figure-eight condition. The peak loads are on the same order of magnitude as those in the extreme braking condition. This conforms to the actual loading situation and validates their application as input loads for subsequent fatigue analysis.

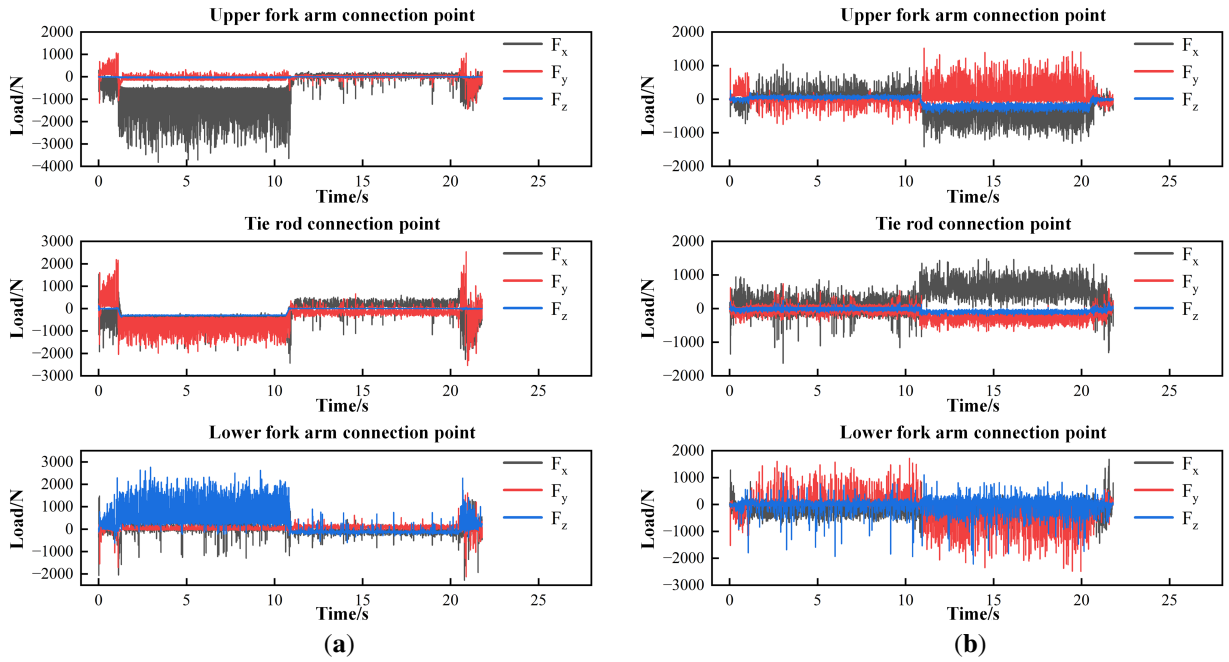


Figure 13: Load spectra of the right front and rear uprights. (**a**) Front upright; (**b**) Rear upright.

3.3 Real Vehicle Test and Load Spectrum Reliability Verification

To verify the accuracy of the load spectra extracted from the multibody dynamics model, a real vehicle figure-eight test is conducted. The limited installation space on the upright makes direct sensor mounting difficult, as it could alter local structural stiffness and affect the load transfer path. Therefore, the left and right damping pushrods are chosen as measurement points for load verification. The force state of the damping pushrods can indirectly reflect the load characteristics of the suspension system. Their open installation space also facilitates sensor placement.

Pressure sensors are installed at the midpoints of the left and right damping pushrods. The real vehicle track strictly replicates the geometric layout shown in Fig. 12. The on-site layout and sensor installation positions are shown in Fig. 14. During the test, the car follows the same driving strategy as the simulation: two laps of right turn followed by two laps of left turn, maintaining constant speed throughout. Real-time force data from the left and right damping pushrods are collected synchronously and compared with the simulation results for verification.



Figure 14: Real vehicle test diagram.

Due to the structural and kinematic symmetry of the figure-eight track, the left and right uprights theoretically experience nearly identical forces. Therefore, the right damping pushrod is chosen for comparative analysis. The measured and simulated loads are compared, as shown in Fig. 15. Fig. 15 demonstrates that the variation trends of the actual and simulated loads exhibit significant consistency, with strong alignment in peak occurrence times and fluctuation patterns.

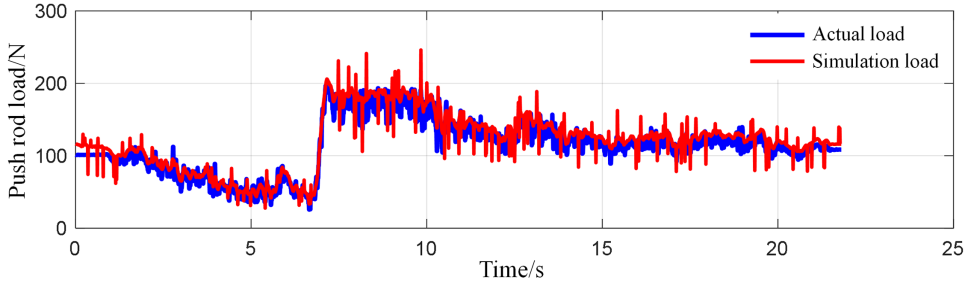


Figure 15: Comparison of actual and simulated loads on the right damping pushrod.

A quantitative analysis is also conducted using statistical indicators such as the Pearson correlation coefficient, data distribution, and relative error. The results are presented in Figs. 16–18. Fig. 16 shows a Pearson correlation coefficient r = 0.9643, indicating a significant linear correlation. Fig. 17 illustrates that the dispersion of the actual and simulated load data is generally consistent, with the median simulated load slightly higher than the measured value. More specifically, the median simulated load exceeds the median measured load by 7.9%. Fig. 18 indicates that the majority of relative errors are around 10%, with a maximum relative error of 30.3%. The overall agreement is satisfactory.

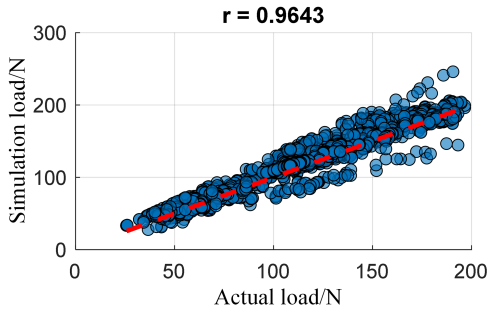


Figure 16: Pearson correlation analysis of actual and simulated loads on the right pushrod.

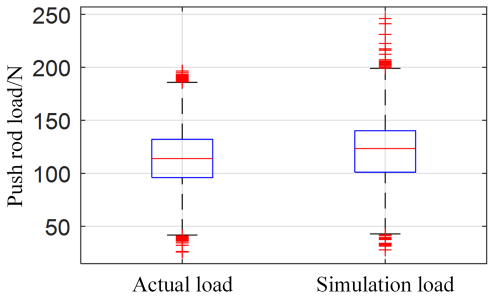


Figure 17: Comparison of data distribution between actual and simulated loads on the right pushrod.

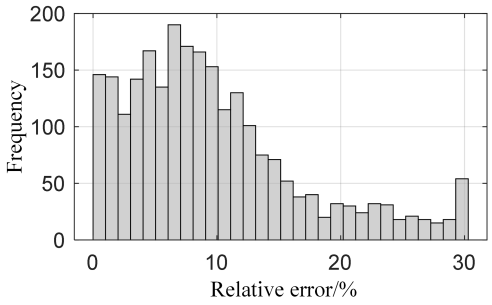


Figure 18: Relative error distribution between actual and simulated loads on the right pushrod.

As the simulated loads exhibit a systematic overestimation relative to the actual forces, the fatigue life predictions derived from these load spectra become inherently conservative, affording an additional safety margin for the design. Accordingly, the indirect validation approach, despite entailing quantifiable load deviations, does not undermine the reliability of the subsequent fatigue assessment.

It should be noted that the present framework provides a comparative and predictive methodology for fatigue life evaluation; however, direct experimental validation of the fatigue predictions through component-level testing of the additively manufactured uprights has not been conducted due to current limitations in testing facilities. The load spectra have been validated by full-vehicle tests (Pearson correlation coefficient r = 0.9643), and the simulated loads are systematically conservative (median overestimation of 7.9%), which inherently provides an additional safety margin. While the validated load spectra and the conservative nature of the predictions lend credibility to the results, full-scale fatigue bench testing of AM uprights under the extracted load spectra is indispensable and will be pursued as the next phase of this research once testing facilities become available.

The established multibody dynamics simulation model demonstrates high reliability. The upright load spectra derived from this model provide high engineering reference value and are applicable for subsequent fatigue investigation.

3.4 Determination of Upright Material ε–N Curve and Fatigue Parameters

Due to limitations in test circumstances, fatigue tests on 7075-T6 aluminum alloy could not be performed. As discussed in Section 3.1, the Manson–Coffin equation (Eq. (3)) inherently unifies the high-cycle and low-cycle regimes within a single framework, making the strain–life (ε–N) approach suitable for the present application. Furthermore, the critical-plane multi-axial fatigue analysis in nCode DesignLife is conventionally coupled with the strain–life formulation and the SWT mean-stress correction model, which represents the standard industrial practice for such components. The fatigue performance parameters of 7075-T6 aluminum alloy are obtained from existing research [40] and listed in Table 4. These fatigue parameters have been cross-validated against the material properties of 7075-T6 aluminum alloy presented in Table 2, and the good agreement confirms their applicability to the present upright geometry and loading regime. Substituting these parameters into the Manson–Coffin equation yields the ε–N curve of 7075-T6 aluminum alloy, as demonstrated in Fig. 19. The curve comprises an elastic segment and a plastic segment and is imported into nCode DesignLife as the material property basis for upright fatigue life forecasting.

3.5 Upright Fatigue Damage Simulation Analysis Based on nCode

Fatigue life analysis of the front and rear uprights is performed via nCode DesignLife. The specific procedure is as follows: finite element analysis results under unit loads for each channel are imported into

the software. These are linearly superimposed with the load spectra of the corresponding channels to obtain the stress–time histories of all upright nodes. Miner's linear damage accumulation rule is used to accumulate damage. The Smith–Watson–Topper (SWT) mean stress correction model is introduced to account for the mean stress effect. The critical plane approach is selected as the multi-axial fatigue damage model to evaluate upright fatigue performance. It should be noted that this fatigue analysis framework relies on several fundamental assumptions. Miner's rule assumes linear damage accumulation and neglects load sequence effects, which is generally accepted for variable amplitude loading of metallic structures when significant overload interactions are absent. The SWT model assumes that the dominant damage mechanism is tensile-mode crack opening, which is consistent with the expected failure mode of the upright under the combined bending and axial loads encountered in service. The critical plane approach further assumes that fatigue damage is controlled by the stress–strain state on a specific material plane, an approach suitable for non-proportional multi-axial loading conditions. These assumptions are widely adopted in engineering practice and are considered appropriate for the present application.

Table 4: Fatigue properties of 7075-T6 aluminum alloy.

Fatigue Strength Coefficient σ_f'/MPA	Fatigue Ductility Coefficient ε_f'	Fatigue Strength Exponent b	Fatigue Ductility Exponent c
1235	0.243	−0.138	−0.710

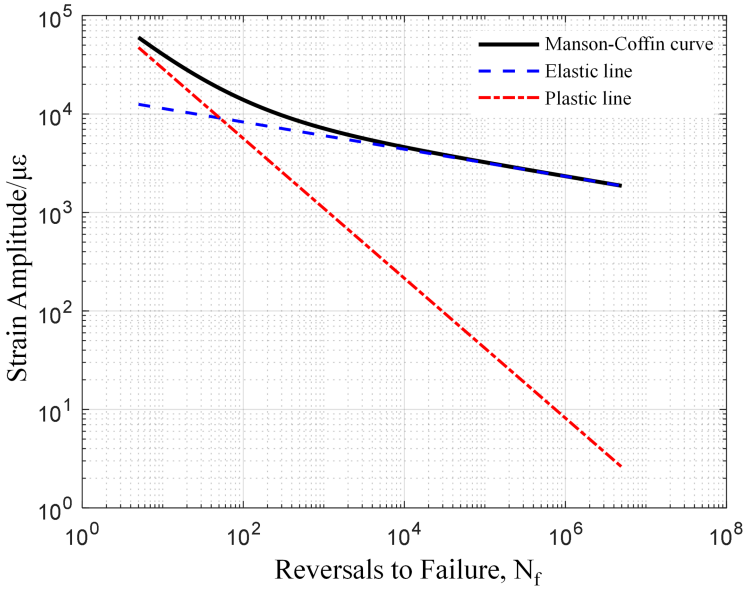
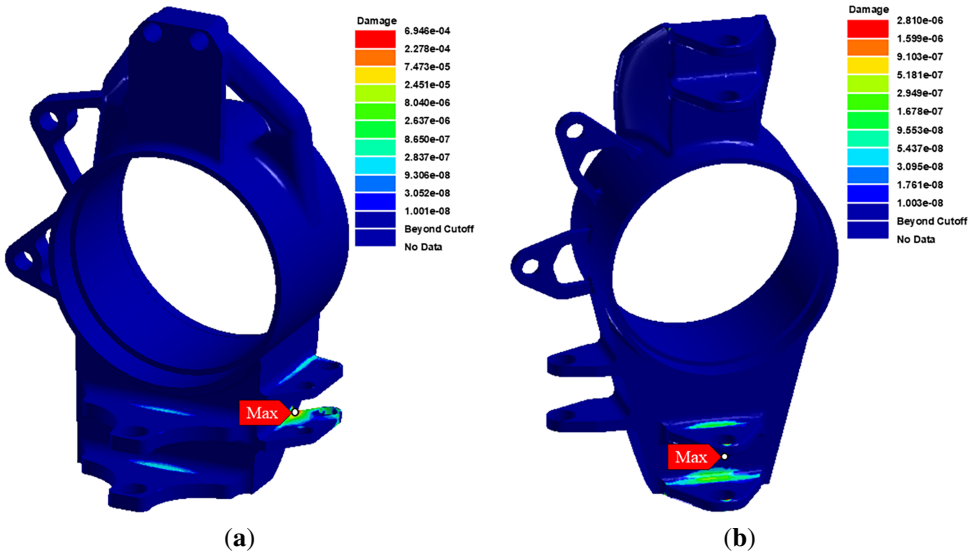


Figure 19: ε–N curve of 7075-T6 aluminum alloy.

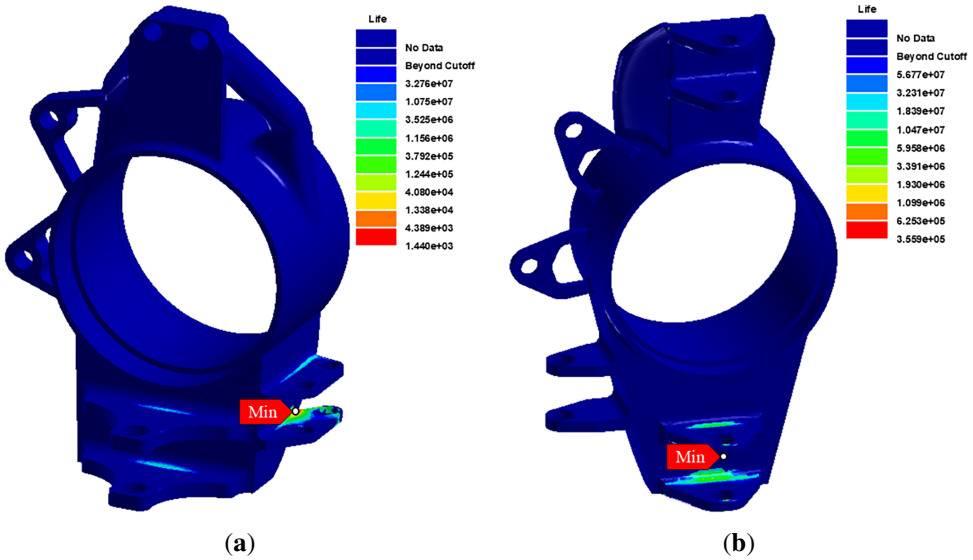
Figs. 20 and 21 show the fatigue damage and fatigue life contours of the front and rear uprights under the figure-eight condition, respectively. Here the fatigue life denotes the number of repetitions of the complete figure-eight load history. Figs. 20 and 21 show that the maximum damage location on the front upright is situated on the rear side of the posterior lug connecting to the steering tie rod. A concentrated damage distribution is observed in this lug region, aligning with theoretical predictions and engineering experience.

The maximum damage location on the rear upright appears near the bolt hole connecting to the lower control arm. The primary high-damage region is located at the connection lug of the lower control arm.



(**a**) (**b**)

Figure 20: Fatigue damage contours of the front and rear uprights under figure-eight conditions. (**a**) Front upright; (**b**) Rear upright.



(**a**) (**b**)

Figure 21: Fatigue life contours of the front and rear uprights under figure-eight conditions. (**a**) Front upright; (**b**) Rear upright.

For further quantitative analysis, the top five nodes with the highest damage values for both the front and rear uprights are listed in Table 5. Table 5 indicates that the peak cumulative damage value for the front upright occurs at node 331,649, measuring 6.95×10^{-4}. For the rear upright, the maximum is at node 40,709, with a value of 2.81×10^{-6}. Both values are far less than 1, fulfilling the criterion of Miner's linear damage accumulation rule, demonstrating that no fatigue failure occurs in the structure.

Table 5: Fatigue analysis results for the front and rear uprights.

Upright	Node	Cumulative Damage	Life/Cycles
Front	331,649	6.95×10^{-4}	1440
	331,650	6.87×10^{-4}	1456
	1,419,779	6.04×10^{-4}	1656
	1,419,778	5.96×10^{-4}	1678
	331,841	5.88×10^{-4}	1701
Rear	40,709	2.81×10^{-6}	3.56×10^{5}
	44,605	2.56×10^{-6}	3.91×10^{5}
	44,960	2.26×10^{-6}	4.43×10^{5}
	224,777	1.55×10^{-6}	6.45×10^{5}
	216,649	1.37×10^{-6}	7.32×10^{5}

4 Fatigue Life Prediction Correction Model Considering Surface Roughness

The traditional ε–N curve is obtained from standard smooth specimens. It fails to account for the influence of surface roughness on actual parts. The direct application of additively manufactured uprights leads to inaccurate fatigue life predictions. This chapter introduces the fatigue notch factor K_f to correct the Manson–Coffin equation. A modified fatigue life model considering surface roughness is established. The influence of surface topography parameters on upright fatigue life is systematically investigated.

4.1 ε–N Curve Correction Method Based on the Fatigue Notch Factor

4.1.1 Calculation of the Surface Fatigue Notch Factor

Research indicates that surface topography gives rise to stress concentration, which further initiates fatigue cracks. When simplifying measured three-dimensional surface topography via two-dimensional surface profiles, the calculated stress concentration factors tend to be overestimated. Unlike three-dimensional surfaces, two-dimensional formulations neglect the Poisson's effect, leading to more conservative predictions that are better suited for engineering product design [30]. Therefore, the AM surface topography was simplified into two-dimensional surface profiles in this paper.

A real surface topography can be decomposed into a superposition of harmonic components using Fourier transform [29]. The surface height function can be articulated as:

$$z(x) = -\sum_{i=1}^{n} A_i \cos\left(2\pi x/\lambda_i + \varphi_i\right) \tag{5}$$

where A_i is the amplitude of the i-th harmonic; λ_i denotes the corresponding wavelength; and φ_i is the phase angle.

The point method of the critical distance theory is adopted to calculate the surface fatigue notch factor K_f. This theory holds that fatigue damage at the notch root is determined by the stress field within a certain characteristic distance ahead of the notch. Combined with the surface topography harmonic expression, the fatigue notch factor calculation formula is [29]:

$$K_f = 1 + 4\pi \sum_{i=1}^{n} \frac{A_i}{\lambda_i} \left(1 - \frac{\pi a_0}{2\lambda_i}\right) e^{-\frac{\pi a_0}{\lambda_i}} \cos\left(\frac{2\pi x_*}{\lambda_i} + \varphi_i\right) \tag{6}$$

where x_* is the coordinate of the notch position; a_0 denotes the material's critical defect size. Its value is related to the material's fatigue crack propagation threshold ΔK_{th} and the fatigue limit $\Delta\sigma_0$ of a mirror-polished specimen.

$$a_0 = \left(\Delta K_{\text{th}}/\Delta\sigma_0\right)^2/\pi \tag{7}$$

The characteristic length a_0 is an intrinsic material parameter that depends solely on the types of material and load ratio [41]. The material characteristic length a_0 varies drastically across different materials, with typical values spanning from micrometers to millimeters [42]. From Eq. (6), a high-frequency cut-off can be defined as $f_{\text{cut-off}} = 2/\left(\pi a_0\right)$. Surface wave components exceeding this cut-off frequency can be discarded, as they exert negligible influence on stress concentration at the reference point [29]. The proposed analytical expression for surface-topography-induced fatigue notch factors has been comprehensively validated through bending and tension-compression fatigue tests [23,43].

4.1.2 Establishment of the Fatigue Life Correction Model

Studies indicate that surface roughness considerably affects fatigue behavior in the high-cycle fatigue region, while its effect on the low-cycle region is rather minimal. Consequently, the correction is predominantly implemented to the elastic part of the ε–N curve [19,23,44]. The fatigue strength exponent b in the Manson–Coffin formula is corrected using the fatigue notch factor K_{f}. The corrected fatigue strength exponent b' and the modified total strain life equation are:

$$b' = b - \frac{1}{7}\log\left(K_{\text{f}}\right) \tag{8}$$

$$\varepsilon_{\text{a}} = \frac{\Delta\varepsilon_{\text{e}}}{2} + \frac{\Delta\varepsilon_{\text{p}}}{2} = \frac{\sigma_{\text{f}}^{'}}{E}\left(2N_{\text{f}}\right)^{b'} + \varepsilon_{\text{f}}^{\prime}\left(2N_{\text{f}}\right)^{c} \tag{9}$$

This model introduces the correction term b', which is related to K_{f} defined in Eq. (6). It enables the quantitative characterization of surface topography effects on high-cycle fatigue life. In the present study, the load spectra and the corresponding strain amplitudes at the critical locations of the upright indicate that the component operates predominantly under high-cycle fatigue conditions. The operational strain levels remain well within the elastic-dominated regime of the material's strain-life curve. Under such circumstances, the fatigue life is governed primarily by the elastic strain component, and the contribution of plastic strain to damage accumulation is minimal. Consequently, applying the correction solely to the fatigue strength exponent introduces negligible error for the current application. It should be noted that, should the strain amplitudes approach the elastic-plastic transition region, leaving the plastic segment unmodified would result in a certain degree of inaccuracy in the low-cycle fatigue regime. However, this situation is not encountered in the upright under the prescribed loading scenarios. The model can be used for upright fatigue life prediction that accounts for micro-scale surface topography.

It should be emphasized that while the present study applies the above surface-topography-corrected fatigue model to the optimized uprights in a parametric and comparative manner, direct component-level experimental validation has not yet been performed due to substantial practical constraints. These include the requirement for a multi-axial fatigue test rig capable of reproducing complex non-proportional load histories, dedicated fixtures that replicate actual suspension boundary conditions without altering load transfer paths, the long testing duration associated with high-cycle fatigue, and the high cost of additive manufacturing and post-processing for full-scale uprights. Nevertheless, the foundational components of the proposed framework have been experimentally validated in prior studies: the critical-distance-based fatigue

notch factor K_f (Eq. (6)) has been verified against bending and tension-compression fatigue tests [23,43], and the K_f-modified Manson–Coffin elastic-segment correction (Eqs. (8) and (9)) has been substantiated through fatigue experiments on machined and additively manufactured metallic specimens [19,23,44]. The present work extends these validated material-level methodologies to complex multi-axial engineering components, with the specific aim of quantitatively revealing how surface topography parameters influence fatigue damage in AM uprights.

4.2 Influence of Surface Topography Parameters on Upright Fatigue Life

The arithmetic mean deviation of the profile, R_a, is the most widely used indicator for evaluating surface roughness in engineering practice and quality control, defined as the arithmetic mean of the absolute distances from the profile points to the mean line within a sampling length. Surface wavelength λ is also selected because, according to the critical distance theory adopted in Eq. (6), the fatigue notch factor K_f is governed by the amplitude-to-wavelength ratio (A_i/λ_i), which determines the local stress concentration induced by surface asperities. While real surfaces contain multiple spatial frequencies, Fourier decomposition allows any complex topography to be represented as a superposition of harmonic waves with distinct wavelengths; thus, λ serves as the fundamental geometric parameter linking micro-scale surface geometry to macroscopic fatigue degradation. To systematically reveal the influence of these primary topography parameters, the upright surface is initially assumed to take the form of a single cosine wave, and the effects of surface wavelength λ and surface roughness R_a on the fatigue life of the upright are investigated separately. It should be noted that other parameters (e.g., skewness, kurtosis, and texture direction) are implicitly embedded in the measured surface topographies discussed in Section 4.3, where two real AM surfaces with identical R_a but different micro-morphologies are shown to produce different fatigue lives.

4.2.1 Influence of Surface Wavelength λ

The surface roughness is fixed as R_a = 5 μm. The surface wavelength λ ranges from 200 to 1000 μm with a step of 200 μm. The fatigue notch factor K_f corresponding to each wavelength is calculated using Eq. (6). The corrected fatigue strength exponent b' is then obtained by substituting K_f into Eq. (8). The fatigue notch factor K_f and corrected fatigue strength exponent b' corresponding to different λ values are listed in Table 6.

Table 6: Fatigue parameters corresponding to different wavelengths λ at R_a = 5 μm.

R_a/μm	λ/μm	K_f	b'
5	200	1.303	−0.154
	400	1.194	−0.149
	600	1.140	−0.146
	800	1.109	−0.144
	1000	1.090	−0.143

Table 6 indicates that when λ = 200 μm, K_f reaches its maximum value of 1.303, simultaneously b' reaches its minimum value of −0.154. As λ increases, K_f gradually decreases and b' gradually increases. When λ = 1000 μm, K_f approaches 1 and b' approaches the original value of −0.138. This is because shorter wavelengths correspond to more sharply varying surface topography. The resulting local stress concentration is more significant, leading to a larger K_f. In contrast, longer wavelengths correspond to a gentler surface and a weaker stress concentration effect.

The modified ε–N curves for different λ values are shown in Fig. 22. Upright fatigue simulations are performed, and the maximum cumulative damage for the front and rear uprights at each λ is shown in Fig. 23.

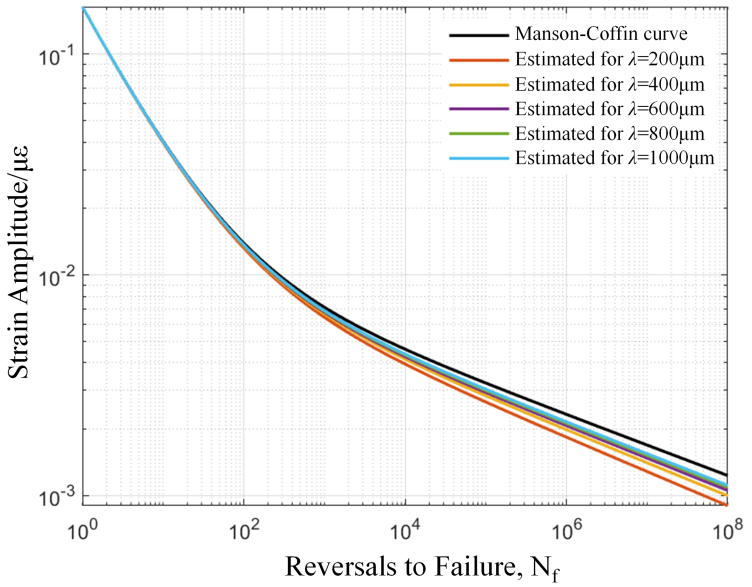


Figure 22: Modified strain-life curves for 7075-T6 aluminum alloy corresponding to different wavelengths λ at R_a = 5 μm.

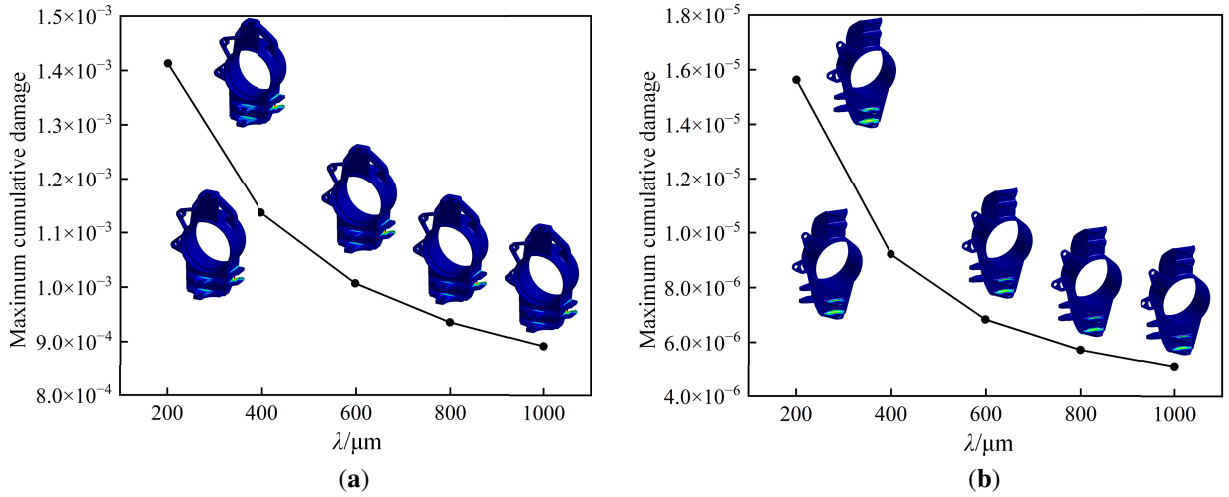


Figure 23: Maximum cumulative damage of the front and rear uprights under different wavelengths λ. (**a**) Front upright; (**b**) Rear upright.

Fig. 22 shows that as λ decreases, the slope change of the elastic segment of the modified ε–N curve becomes more pronounced. The curve in the high-cycle fatigue region shifts downward more significantly. The predicted fatigue life under the same strain amplitude is lower. This indicates that surfaces with short wavelengths have a more severe degrading effect on high-cycle fatigue performance. Fig. 23 shows that the maximum cumulative damage of both the front and rear uprights decreases with increasing λ. When λ = 200 μm, the maximum cumulative damage is 1.413×10^{-3} for the front upright and 1.563×10^{-5} for the

rear upright. When λ = 1000 μm, these values decrease to 8.901×10^{-4} and 5.087×10^{-6}, respectively. This indicates that for a fixed R_a, a shorter wavelength leads to more severe fatigue damage and lower fatigue life.

4.2.2 Influence of Surface Roughness R_a

Although the idealized sinusoidal surface profile adopted herein represents a simplification of the stochastic morphology encountered on real additively manufactured surfaces, the selected R_a range (20–100 μm) is consistent with experimentally reported surface roughness values for aluminum alloys produced by laser powder bed fusion. As documented in the literature, the as-built surface roughness R_a can reach up to 80 μm or higher, while post-processed surfaces typically fall within the 10–30 μm range [45]. Therefore, the parametric investigation covers conditions spanning from well-finished to as-built AM surface states, and the qualitative trends revealed remain of practical relevance for guiding surface finish optimization in fatigue-critical AM components.

The surface wavelength is fixed at λ = 1000 μm. The surface roughness R_a ranges from 20 to 100 μm, with a step of 20 μm. The K_f and b' values corresponding to different R_a are listed in Table 7.

Table 7: Fatigue parameters corresponding to different roughness values at λ = 1000 μm.

λ/μm	R_a/μm	K_f	b'
1000	20	1.359	−0.157
	40	1.718	−0.172
	60	2.077	−0.183
	80	2.436	−0.193
	100	2.795	−0.202

Table 7 shows that when R_a = 20 μm, K_f = 1.359 and b' = −0.157. As R_a increases, K_f increases and b' decreases. When R_a = 100 μm, K_f rises to 2.795 and b' drops to −0.202. This is because a larger R_a means greater amplitude of surface micro-fluctuations. The resulting local stress concentration is more significant, leading to a larger K_f.

The modified ε–N curves for different R_a are shown in Fig. 24. Upright fatigue simulations are performed, and the maximum cumulative damage at each R_a is shown in Fig. 25. Fig. 24 shows that as R_a grows, the slope alteration of the elastic segment of the modified ε–N curve becomes more pronounced. The curve in the high-cycle fatigue region shifts downward more significantly. The anticipated fatigue life under the identical strain amplitude decreases. When R_a = 100 μm, the downward shift is most pronounced, indicating that high-roughness surfaces exert a substantial detrimental impact on high-cycle fatigue performance. Fig. 25 shows that the maximum cumulative damage of both the front and rear uprights increases with increasing R_a. When R_a = 20 μm, the maximum cumulative damage is 1.559×10^{-3} for the front upright and 1.997×10^{-5} for the rear upright. When R_a = 100 μm, these values increase to 6.477×10^{-3} and 5.124×10^{-4}, respectively. This signifies that for a constant surface wavelength λ, a larger R_a leads to more severe fatigue damage and lower fatigue lifespan. Therefore, reducing R_a through processes such as polishing can effectively enhance the fatigue performance of the upright.

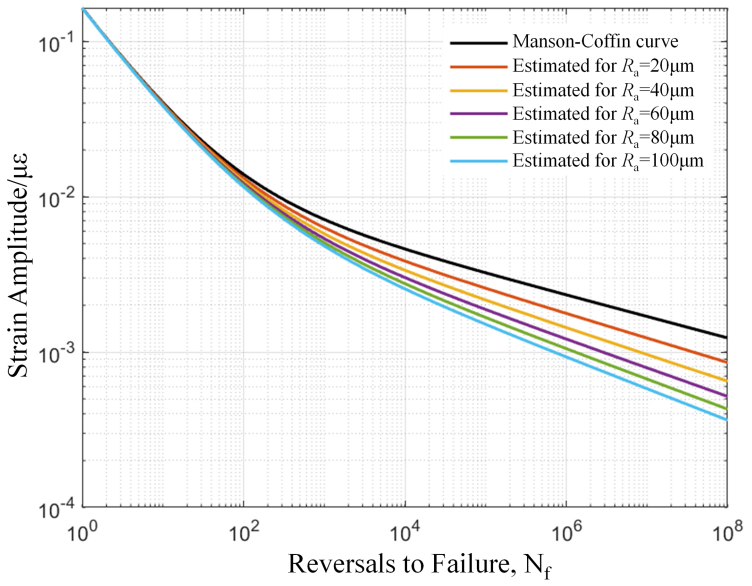


Figure 24: Modified strain-life curves for 7075-T6 aluminum alloy corresponding to different surface roughness values R_a at λ = 1000 μm.

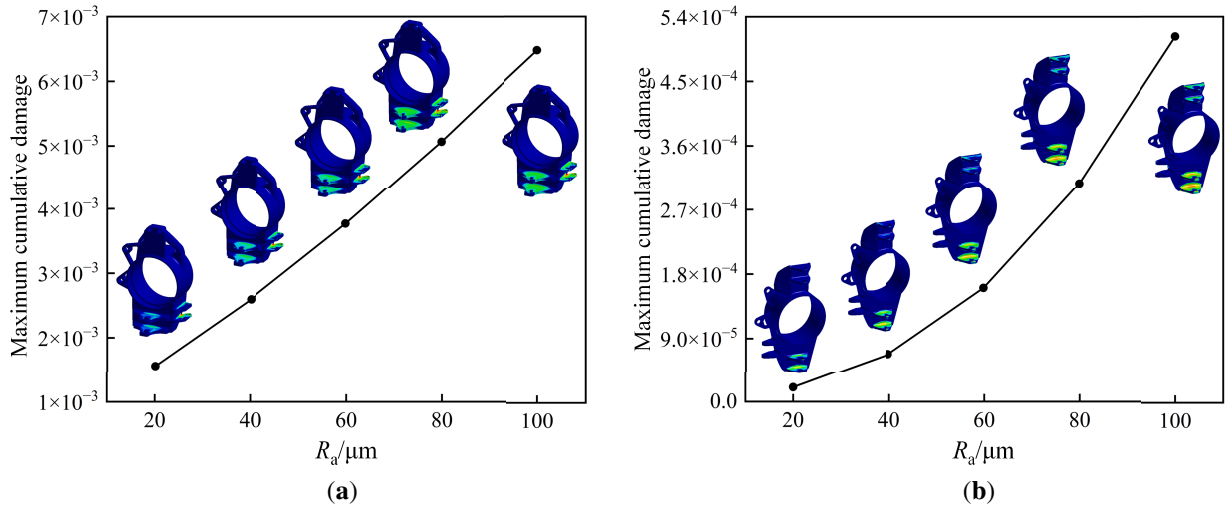


Figure 25: Maximum cumulative damage of the front and rear uprights under different surface roughness values R_a. (**a**) Front upright; (**b**) Rear upright.

4.3 Influence of Measured Surface Topography on Upright Fatigue Life

Actual additively manufactured surface topographies exhibit complex random features that are challenging to describe with a singular cosine wave. Two measured additively manufactured surface topographies, both with R_a = 25 μm, are selected. It should be noted that these surface topographies were acquired from a flat witness coupon fabricated using the same material and additive manufacturing process as the uprights, rather than extracted directly from the upright surfaces. This separate coupon-based measurement avoids any interference with the load-bearing geometry and ensures representative characterization of the as-built surface condition. The surface topographies are reconstructed using Fourier series and subjected

to high-pass filtering to remove high-frequency components that have negligible effect on fatigue performance [29]. The two measured surface topographies are shown in Fig. 26. Surface roughness measurements entail uncertainties from instrumental resolution, sampling area, and filtering cut-off wavelength. In this study, measurements were performed following a standardized procedure with a consistent protocol to ensure comparability. While these uncertainties may affect the absolute magnitudes of predicted fatigue lives, the relative trends among different surface conditions and the qualitative conclusions remain robust.

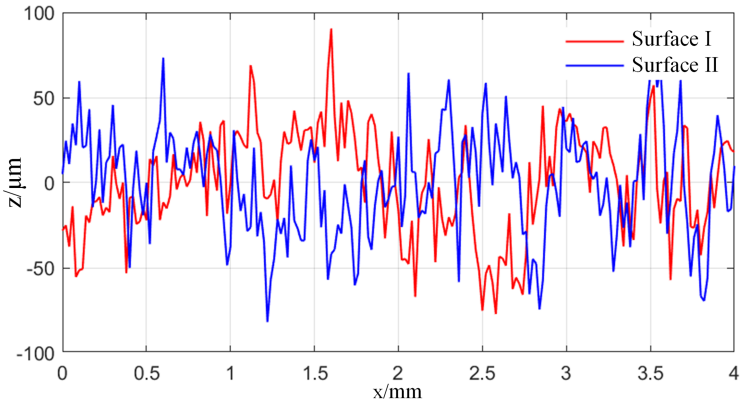


Figure 26: Two measured surface topographies.

The effective fatigue notch factor $\overline{K}_f$ for each surface is taken as the average of the top 10 points with the largest K_f values on that surface. The calculated values of $\overline{K}_f$ and the corrected fatigue strength exponent b' are listed in Table 8.

Table 8: Fatigue parameters of the two measured surfaces.

Surface	R_a/μm	$\overline{K}_f$	b'
I	25	1.391	−0.158
II		1.482	−0.162

The modified ε–N curves corresponding to the two measured surfaces are shown in Fig. 27. The upright fatigue cumulative damage contours for both surfaces are shown in Fig. 28.

Fig. 27 reveals that despite both surfaces having an R_a of 25 μm, their micro-geometric features are distinctly different. Surface I has relatively gentle undulations with a uniform distribution of peaks and valleys. Surface II has sharply undulating features with obvious sharp grooves, which are prone to cause severe stress concentration. Table 8 shows that the effective fatigue notch factor $\overline{K}_f$ of Surface II is 1.482, larger than the 1.391 of Surface I. The corrected fatigue strength exponent b' of Surface II is −0.162, which is less than the −0.158 of Surface I. Fig. 27 shows that in the high-cycle fatigue region, the modified ε–N curve for Surface II shifts downward more than that for Surface I. This indicates a more significant degradation of fatigue performance by Surface II.

Fig. 28 shows that for the front upright, the maximum cumulative damage is 1.645×10^{-3} for the Surface I and 1.872×10^{-3} for the Surface II. This result fully demonstrates that even with the same R_a, surfaces with different micro-topographies can have significantly different effects on fatigue performance. Using only R_a as a surface quality evaluation index has limitations. The influence of micro-geometric features on fatigue performance must be comprehensively considered.

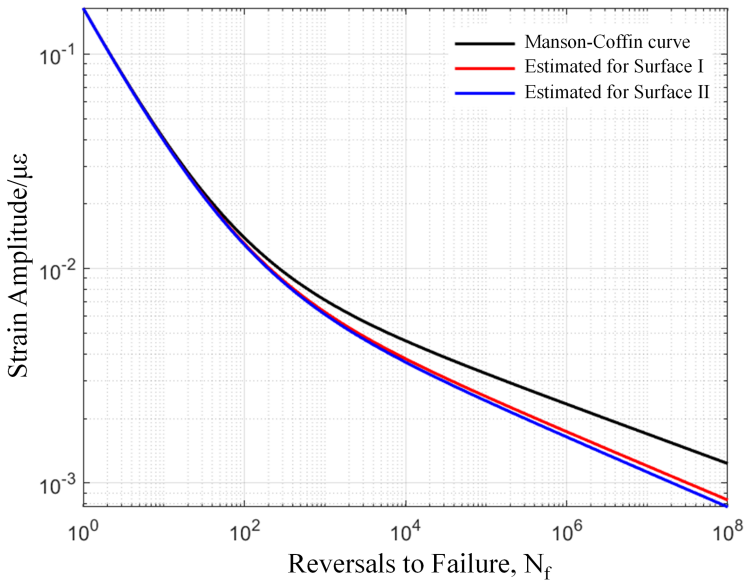


Figure 27: Modified strain-life curves for the two measured surfaces.

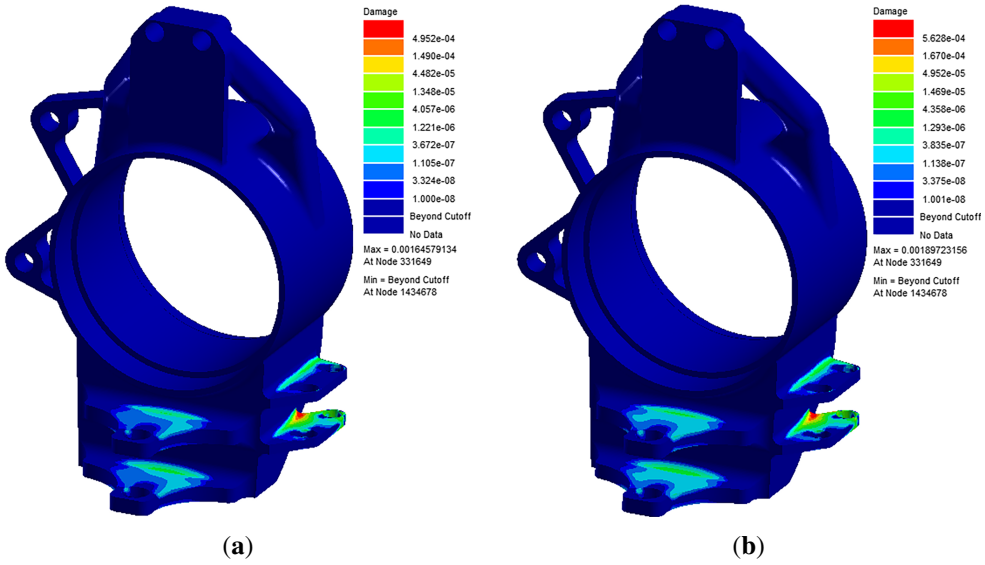


Figure 28: Fatigue cumulative damage contours of the front upright for measured surfaces I and II. (**a**) Measured surface I; (**b**) Measured surface II.

The above findings unequivocally validate the viability and superiority of the proposed approach in AM lightweight components. The integrated design framework and its closed-loop workflow have been detailed in Section 2 (see Fig. 1) and rigorously comply with relevant engineering design criteria.

5 Conclusions

This paper takes the front and rear uprights of an FSC racing car as the research object. A systematic investigation is conducted on topology optimization design and fatigue life estimation, considering micro-scale surface topography. A complete technical framework is established, encompassing topology

optimization, load acquisition, fatigue analysis, and life correction. The principal findings of this article are as follows:

(1) An integrated design and verification process combining topology optimization, multibody dynamics load acquisition, and fatigue life prediction is proposed and validated. Early incorporation of additive manufacturing process constraints circumvents the inefficiencies of repeated late-stage corrections typical of smooth-model-based designs, while mutual validation of multibody dynamics simulation and real vehicle tests addresses the inaccuracy of load inputs derived solely from simulations or empirical estimates. In contrast to conventional workflows that treat fatigue evaluation as a post-processing step disconnected from early design, and to the defect-driven TopFat method which pioneered AM defect integration but did not unify load spectrum extraction, multi-axial fatigue calculation, and surface topography correction, the present framework establishes a complete closed-loop engineering chain from conceptual design to reliable fatigue life prediction for AM safety-critical components.

(2) The influence of additively manufactured surface topography on structural fatigue life is systematically revealed, and a generalizable K_f-modified Manson–Coffin strain-life model is established. Fatigue damage is co-determined by arithmetic roughness R_a and surface spatial wavelength; shorter wavelengths and higher roughness amplify stress concentration and degrade high-cycle durability. Critically, identical R_a values with different micro-topography morphologies produce significantly different fatigue lifetimes, invalidating the conventional single-indicator surface quality standard. Quantitatively, reducing the wavelength from 1000 to 200 μm at R_a = 5 μm increases K_f from 1.090 to 1.303 and raises maximum damage by approximately 59% (front upright); increasing R_a from 20 to 100 μm at a fixed 1000 μm wavelength elevates K_f from 1.359 to 2.795 and amplifies maximum damage by over 300% (front upright). These component-level trends align with material-level findings in prior specimen-based studies and extend the surface topography correction methodology to complex multi-axial engineering components, confirming the inadequacy of relying solely on R_a for fatigue-oriented surface quality control.

The integrated design framework and surface topography fatigue correction model developed in this work supply systematic theoretical fundamentals and operable engineering workflows for lightweight optimization and accurate fatigue durability assessment of generic AM safety-critical load-carrying structures, covering new energy vehicle chassis knuckles, aerospace connecting lugs and humanoid robot joint supports. The FSC racing upright acts as a multi-axial cyclic load validation specimen to demonstrate the full technical pipeline, and the presented methods can be directly transplanted to cross-domain AM structural development with corresponding material fatigue parameter substitution. The research outcomes facilitate the reliable industrial deployment of additive manufacturing for fatigue-sensitive lightweight components.

Acknowledgement: The authors thank the MEIYING Formula Racing Team for providing experimental support.

Funding Statement: This study was supported by Shenzhen Science and Technology Program (Grant No. 20231128093312001), Shenzhen Polytechnic Research Fund (Grant No. 6024310039k), and Guangdong Basic and Applied Basic Research Foundation (No. 2023A1515240032).

Author Contributions: The authors confirm contribution to the paper as follows: investigation, methodology and validation: Yuwei Liu, Yuhui Liu, Lulu Nie; analysis and interpretation of results: Yuwei Liu, Yuhui Liu, Zhengkun Cheng, Yang Zhao; draft manuscript preparation: Yuwei Liu, Yuhui Liu; conceptualization, visualization, supervision, writing—review & editing: Zhengkun Cheng. All authors reviewed and approved the final version of the manuscript.

Availability of Data and Materials: The data that support the findings of this study are available from the corresponding author upon reasonable request.

Ethics Approval: Not applicable.

Conflicts of Interest: The authors declare no conflicts of interest.

Abbreviations

The following abbreviations are used in this manuscript

A_i	Amplitude of the i-th harmonic
a_0	The material's critical defect size
b	Fatigue strength exponent
b'	Corrected fatigue strength exponent
$C_w(\rho)$	Total weighted compliance
c	Fatigue ductility exponent
D	The cumulative damage
E	The material's elastic modulus
$E(\rho_i)$	Interpolated elastic modulus of the element
E_0	Initial elastic modulus of the material
$E_{\min}$	A very small elastic modulus
$\mathbf{F}_k$	Global load vector for the k-th load case
f_v	Volume fraction constraint
K_f	Fatigue notch factor
$\overline{K}_f$	Effective fatigue notch factor
$\mathbf{K}(\rho)$	Global stiffness matrix
N_f	Fatigue life
p	Penalty factor
R_a	The arithmetic mean deviation of the profile
$\mathbf{U}_k$	Nodal displacement vector for the k-th load case
$V(\rho)$	Optimized structural volume
V_0	Total volume of the initial design domain
w_k	The weighting factor for the k-th load case
x_*	The coordinate of the notch position
ρ_i	The element relative density
$\rho_{\min}$	Minimum relative density
ε_a	Total strain amplitude
ε_f'	Fatigue ductility coefficient
σ_f'	Fatigue strength coefficient
λ_i	The corresponding wavelength
φ_i	The phase angle
AM	Additive manufacturing
ε–N	Strain Life
FE	Finite element
FSC	Formula Student China
SIMP	Solid isotropic material with penalty

References

1. Liu J, Gaynor AT, Chen S, Kang Z, Suresh K, Takezawa A, et al. Current and future trends in topology optimization for additive manufacturing. Struct Multidiscip Optim. 2018;57(6):2457–83. doi:10.1007/s00158-018-1994-3.
2. Zhu J, Zhou H, Wang C, Zhou L, Yuan S, Zhang W. A review of topology optimization for additive manufacturing: status and challenges. Chin J Aeronaut. 2021;34(1):91–110. doi:10.1016/j.cja.2020.09.020.

3. Lazarov BS, Wang F, Sigmund O. Length scale and manufacturability in density-based topology optimization. Arch Appl Mech. 2016;86(1):189–218. doi:10.1007/s00419-015-1106-4.
4. Deaton JD, Grandhi RV. A survey of structural and multidisciplinary continuum topology optimization: post 2000. Struct Multidiscip Optim. 2014;49(1):1–38. doi:10.1007/s00158-013-0956-z.
5. Talay E, Özkan C, Gürtaş E. Designing lightweight diesel engine alternator support bracket with topology optimization methodology. Struct Multidiscip Optim. 2021;63(5):2509–29. doi:10.1007/s00158-020-02812-z.
6. Liu B, Yang J, Zhang X, Li X. Topology optimization and lightweight platform development of pure electric vehicle frame-type aluminum body considering crash performance. J Mater Eng Perform. 2025;34(3):2424–34. doi:10.1007/s11665-024-09239-3.
7. Cui B, Long K, Saeed A, Guo N, Wu G, Zhang H. Design methodology for self-similar modular assembly lattice-type wind turbine supporting structures using topology optimization. Comput Model Eng Sci. 2026;146(3):9. doi:10.32604/cmes.2026.078151.
8. Chen Z, Long K, Zhang C, Yang X, Lu F, Wang R, et al. A fatigue-resistance topology optimization formulation for continua subject to general loads using rainflow counting. Struct Multidiscip Optim. 2023;66(9):210. doi:10.1007/s00158-023-03658-x.
9. Chen Z, Long K, Wen P, Nouman S. Fatigue-resistance topology optimization of continuum structure by penalizing the cumulative fatigue damage. Adv Eng Softw. 2020;150(2):102924. doi:10.1016/j.advengsoft.2020.102924.
10. Lu F, Long K, Zhang C, Zhang J, Tao T. A novel design of the offshore wind turbine tripod structure using topology optimization methodology. Ocean Eng. 2023;280(2):114607. doi:10.1016/j.oceaneng.2023.114607.
11. Jiang W, Zhang Y, Liu J, Zhang D, Yan Y, Song C. Multi-objective optimization design for steel-aluminum lightweight body of pure electric bus based on RBF model and genetic algorithm. Electron Res Arch. 2023;31(4):1982–97. doi:10.3934/era.2023102.
12. Lu Y, Mao H, Zhou M. Topology optimization of electric vehicle chassis structure with distributed load-bearing batteries. Struct Multidiscip Optim. 2023;66(6):134. doi:10.1007/s00158-023-03578-w.
13. Zhang J, Ning L, Hao Y, Sang T. Topology optimization for crashworthiness and structural design of a battery electric vehicle. Int J Crashworthiness. 2021;26(6):651–60. doi:10.1080/13588265.2020.1766644.
14. Vayssette B, Saintier N, Brugger C, El May M, Pessard E. Numerical modelling of surface roughness effect on the fatigue behavior of Ti-6Al-4V obtained by additive manufacturing. Int J Fatigue. 2019;123(1):180–95. doi:10.1016/j.ijfatigue.2019.02.014.
15. Abroug F, Ma Y, Mokhtari M, Arnaud L, Hor A, Keller C. Effect of re-lasing on the fatigue properties of 316L stainless steel produced by laser powder bed fusion. Procedia Struct Integr. 2024;57(3):87–94. doi:10.1016/j.prostr.2024.03.011.
16. Elambasseril J, Rogers J, Wallbrink C, Munk D, Leary M, Qian M. Laser powder bed fusion additive manufacturing (LPBF-AM): the influence of design features and LPBF variables on surface topography and effect on fatigue properties. Crit Rev Solid State Mater Sci. 2023;48(1):132–68. doi:10.1080/10408436.2022.2041396.
17. Shrestha R, Simsiriwong J, Shamsaei N. Fatigue behavior of additive manufactured 316L stainless steel parts: effects of layer orientation and surface roughness. Addit Manuf. 2019;28:23–38. doi:10.1016/j.addma.2019.04.011.
18. Xu Y, Chen H, Zhang S, He T, Liu X, Chang X. An experimental study on low-cycle fatigue crack initiation life prediction of powder superalloy FGH96 based on the Manson-Coffin and damage mechanics methods. Metals. 2021;11(3):489. doi:10.3390/met11030489.
19. Yu H, Liu X, Yang G, Zhang X, Lai J, Wei Y. An improved Manson–Coffin model for fatigue life prediction of large crude oil storage tanks via environment temperature and surface roughness. J Braz Soc Mech Sci Eng. 2024;46(4):208. doi:10.1007/s40430-024-04793-2.
20. Wang Y, Wang X, Liu Z, Liu S, Wang S, Chen H, et al. A plastic strain energy method exploration between machined surface integrity evolution and torsion fatigue behaviour of low alloy steel. Chin J Aeronaut. 2022;35(10):412–29. doi:10.1016/j.cja.2021.11.003.
21. Hebert J, Khonsari MM. Effect of surface roughness and polishing orientation on fatigue life and fracture fatigue entropy. Fatigue Fract Eng Mat Struct. 2024;47(5):1514–30. doi:10.1111/ffe.14260.

22. Karabudak F, Şüküroğlu EE, Şüküroğlu S, Yeşildal R. The effect of surface roughness on fatigue life in AZ31 magnesium alloy. Trans Indian Inst Met. 2023;76(11):3095–103. doi:10.1007/s12666-023-03088-9.
23. Zhu X, Dong Z, Zhang Y, Cheng Z. Fatigue life prediction of machined specimens with the consideration of surface roughness. Materials. 2021;14(18):5420. doi:10.3390/ma14185420.
24. Wang H, Liu X, Wu Q, Wang X, Wang Y. An improved fatigue life prediction model for shock absorber cylinder with surface roughness correction. Eng Comput. 2021;38(6):2713–32. doi:10.1108/ec-05-2020-0263.
25. Murakami Y, Endo M. Effects of defects, inclusions and inhomogeneities on fatigue strength. Int J Fatigue. 1994;16(3):163–82. doi:10.1016/0142-1123(94)90001-9.
26. Wang Y, Li T, Xu H. Effect of stress concentration caused by 3D surface topography on gear bending fatigue life. Eng Res Express. 2025;7(4):045526. doi:10.1088/2631-8695/ae0f00.
27. Zhang W, Zhu Z, Zheng M, Su P. Fatigue life study of milled surfaces based on stress concentration factor. Surf Topogr Metrol Prop. 2025;13(1):015013. doi:10.1088/2051-672X/adad04.
28. Kozáková K, Klusák J. Fatigue lifetime predictions of notched specimens based on the critical distance and stress concentration factors. Theor Appl Fract Mech. 2024;133(6):104579. doi:10.1016/j.tafmec.2024.104579.
29. Cheng Z, Liao R, Lu W, Wang D. Fatigue notch factors prediction of rough specimen by the theory of critical distance. Int J Fatigue. 2017;104:195–205. doi:10.1016/j.ijfatigue.2017.07.004.
30. Liu Y, Liu Y, Cheng Z. Investigating the effects of surface texture direction and Poisson's ratio on stress concentration factors. Materials. 2025;18(10):2260. doi:10.3390/ma18102260.
31. Risaliti E, Tamarozzi T, Vermaut M, Cornelis B, Desmet W. Multibody model based estimation of multiple loads and strain field on a vehicle suspension system. Mech Syst Signal Process. 2019;123:1–25. doi:10.1016/j.ymssp.2018.12.024.
32. Kamal M, Rahman MM, Rahman AGA. Fatigue life evaluation of suspension knuckle using multibody simulation technique. J Mech Eng Sci. 2012;3:291–300. doi:10.15282/jmes.3.2012.5.0027.
33. Kashyzadeh KR, Farrahi GH. Improvement of HCF life of automotive safety components considering a novel design of wheel alignment based on a Hybrid multibody dynamic, finite element, and data mining techniques. Eng Fail Anal. 2023;143(2):106932. doi:10.1016/j.engfailanal.2022.106932.
34. Li D, Tian J, Shi S, Wang S, Deng J, He S. Lightweight design of commercial vehicle cab based on fatigue durability. Comput Model Eng Sci. 2023;136(1):421–45. doi:10.32604/cmes.2023.024133.
35. Li J, Tan J, Dong J. Lightweight design of front suspension upright of electric formula car based on topology optimization method. World Electr Veh J. 2020;11(1):15. doi:10.3390/wevj11010015.
36. Zoroufi M, Fatemi A. Experimental durability assessment and life prediction of vehicle suspension components: a case study of steering knuckles. Proc Inst Mech Eng Part D J Automob Eng. 2006;220(11):1565–79. doi:10.1243/09544070jauto310.
37. Niutta CB, Tridello A, Barletta G, Gallo N, Baroni A, Berto F, et al. Defect-driven topology optimization for fatigue design of additive manufacturing structures: application on a real industrial aerospace component. Eng Fail Anal. 2022;142(11):106737. doi:10.1016/j.engfailanal.2022.106737.
38. Almonti D, Salvi D, Mingione E, Vesco S. Lightweight and sustainable steering knuckle via topology optimization and rapid investment casting. J Manuf Mater Process. 2025;9(8):252. doi:10.3390/jmmp9080252.
39. Kaufman JG. Properties of aluminum alloys: tensile, creep, and fatigue data at high and low temperatures. Materials Park, OH, USA: ASM International; 1999.
40. Chiocca A, Sgamma M, Frendo F, Bucchi F, Marulo G. Fatigue assessment of a FSAE car rear upright by a closed form solution of the critical plane method. Fract Struct Integr. 2024;18(67):153–62. doi:10.3221/igf-esis.67.11.
41. El Haddad MH, Topper TH, Smith KN. Prediction of non propagating cracks. Eng Fract Mech. 1979;11(3):573–84. doi:10.1016/0013-7944(79)90081-x.
42. Taylor D. Analysis of fatigue failures in components using the theory of critical distances. Eng Fail Anal. 2005;12(6):906–14. doi:10.1016/j.engfailanal.2004.12.007.
43. Weber F, Starke P. Implementation of modelled surface roughness in the accelerated lifetime prediction of a 20MnMoNi5-5 steel. Int J Fatigue. 2024;186(4):108391. doi:10.1016/j.ijfatigue.2024.108391.

44. Lee S, Pegues JW, Shamsaei N. Fatigue behavior and modeling for additive manufactured 304L stainless steel: the effect of surface roughness. Int J Fatigue. 2020;141:105856. doi:10.1016/j.ijfatigue.2020.105856.
45. Calignano F, Manfredi D, Ambrosio EP, Iuliano L, Fino P. Influence of process parameters on surface roughness of aluminum parts produced by DMLS. Int J Adv Manuf Technol. 2013;67(9):2743–51. doi:10.1007/s00170-012-4688-9.